ChemComm

FEATURE ARTICLE

View Article Online
View Journal | View Issue

Cite this: *Chem. Commun.*, 2025, **61**, 16738

Concurrent utilization of e^- and h^+ for water splitting to H_2 and biomass components into value-added products: sustainable solar-driven photocatalysis towards meeting SDG7, 12 and 13

Sivaraj Rajendran,[a] Simi Saju,[a] Thomas Mathew[a] and Chinnakonda S. Gopinath *[bc]

Photocatalytic water splitting is considered one of the efficient methods for producing green hydrogen. However, the sluggish oxygen evolution reaction (OER) kinetics with four electrons limits the overall efficiency of water splitting. Biomass components/biomass derivatives are renewable carbon feedstocks that are abundantly available in nature. It is prudent to make use of electrons and holes concurrently in photocatalysis for H_2 production and oxidation of biomass components, respectively, due to the latter's occurrence at a lower potential ($\leq$1 V) than that of the OER (>1.23 V), to value-added products (VAPs); this approach makes the entire process energy-efficient and kinetically superior. This potential approach could effectively utilize the charge carriers and abundant renewable resources of water and biomass simultaneously, meeting the sustainability, energy conversion and economic goals together. Parallel utilization of the charge carriers for redox reactions also enhances the sustainability of the catalyst system employed. Interestingly, biomass component oxidation to VAPs occurs in several steps, which not only enhances hole utilization but also provides an opportunity to design better catalysts to enhance the selectivity of the target products. Carrying out such reactions under aerobic or anaerobic conditions and different pH conditions allows fine-tuning of the product selectivity. The current review provides a detailed overview of the recent developments in this emerging area with three different types of photocatalyst systems, namely, oxide-, chalcogenide-, and carbon-based materials. Among these, the oxide-based systems generally demonstrate the highest activity with sustainability, maintaining performance for several hours. While many of these systems exhibited high selectivity towards a single product, 100% selectivity to lactic acid from glycerol was observed with a $BiVO_4$-integrated TiO_2 catalyst. Finally, the challenges, opportunities and future perspectives in this thriving field are listed, and they underscore the role of a carbon-neutral economy towards achieving a potentially sustainable future.

Received 18th July 2025,
Accepted 23rd September 2025

DOI: 10.1039/d5cc04056f

rsc.li/chemcomm

1. Introduction

Energy crises and environmental issues are two of the major global challenges in the present world. Energy produced by the conventional fossil fuel route is not sustainable, and it is insufficient to meet the ever-increasing energy demands.[1,2] The development of green and sustainable energy solutions from renewable resources has become a necessity, and researchers worldwide have been working towards this goal for the past few decades.[3,4] Green hydrogen has gained enormous attention within the last decade across the globe due to its high combustion energy and no associated carbon emission.[5–7] At present, nearly the entire amount of H_2 used for oil-refining and chemical industry applications is generated from one of the fossil fuel-based technologies such as steam methane reforming (SMR) and coal gasification.[8] However, these processes inevitably emit a huge amount of CO_2 (12–20 kg per kg of H_2), and hence, this is called grey hydrogen. A very recent review[9] from the IEA (International Energy Agency) underscores that the H_2 demand is still highly concentrated in traditional refining and chemical sectors; demand from any new sector, especially for green hydrogen, is yet to pick-up, and a critical reason is the high cost. Therefore, it is highly essential

[a] *Department of Chemistry, St. John's College (Affil. University of Kerala), Anchal, Kerala-691306, India*
[b] *Catalysis and Inorganic Chemistry Division, CSIR – National Chemical Laboratory, Dr Homi Bhabha Road, Pune 411 008, India. E-mail: cs.gopinath@ncl.res.in, csgopinaath@gmail.com*
[c] *Department of Chemistry, Indian Institute of Technology Palakkad, Kanjikode, Palakkad 678 623, India*

to develop viable technologies for the production of green H_2 *via* non-polluting, economical as well as sustainable routes, which is indeed a grand challenge.[10]

Water splitting by photocatalysis or electrolysis, compared to currently practiced steam methane reforming, offers an alternate pathway for generating green H_2. However, the high overpotential on the top of anodic minimum potential of 1.23 V for the oxygen evolution reaction (OER) remains a critical challenge. It is to be noted that although ~33.3 kWh per kg H_2 energy output is possible, 50–60 kWh of renewable electricity input is required in electrolysis methods to produce 1 kg of H_2; this gap between the output and the input energy needs to be addressed immediately. One promising approach to address the large overpotential of the OER is to replace the same with organic oxidation reactions, such as the oxidation of biomass-derived components like glycerol and glucose.[5,10] These reactions occur at significantly lower potentials ($\leq$1.0 V *vs.* RHE), and the biomass component oxidation generates value-added products (VAPs). Hence, the OER could be completely avoided, and many semiconductor photocatalysts with a lower oxidation potential can also be deployed suitably. Integrating H_2 production with the oxidation of biomass-derived components to VAPs exemplifies a novel strategy for advancing the circular economy and enhancing the efficiency of the overall reaction; a critical

Sivaraj Rajendran

Sivaraj Rajendran received his Bachelor's degree and Master's degree in chemistry from the University of Kerala, Trivandrum. He is presently a PhD student at the Department of Chemistry, St. John's College, Anchal, affiliated to the University of Kerala, Trivandrum, under the supervision of Dr Thomas Mathew. His research interest mainly focuses on the design of transition metal-based nanomaterials for a wide variety of photocatalytic and electrocatalytic applications such as water splitting, biomass conversion, and CO_2 reduction.

Simi Saju

Ms Simi Saju received her Bachelor's degree and Master's degree in chemistry from the University of Kerala, Trivandrum. She is presently a PhD student at the Department of Chemistry, St. John's College, Anchal, affiliated to the University of Kerala, Trivandrum under the supervision of Dr Thomas Mathew. Currently, she is the HoD and Assistant Professor at the Department of Chemistry, St. John's College, Anchal. She is actively involved in teaching chemistry and interdisciplinary topics at graduate and post-graduate levels. Her research interest mainly focuses on the design of transition metal-based nanomaterials for steam reforming, CO_2 utilization and RWGS reaction.

Thomas Mathew

Thomas Mathew completed his PhD in 2003 at NCL, Pune. He gained postdoctoral experience from AIST, Japan, Academia Sinica, Taiwan, JSPS Fellow at the University of Tokyo, and 3 years of industrial research experience at Toyota Central R&D Labs, Japan. He also received an HRSMC Fellowship to perform research at the University of Amsterdam, The Netherlands. He has been an Assistant Professor since 2013 at St. John's College, India. He has published more than 40 research articles and 2 patents. He is actively involved in teaching chemistry at graduate and post-graduate levels. His research interest includes heterogeneous catalysis, photocatalysis, electrocatalysis, steam reforming, CO_2 utilization and RWGS reaction.

Chinnakonda S. Gopinath

Chinnakonda S. Gopinath (Gopi) completed his PhD in 1993 at IIT Madras. After three post-doc stints, Gopi joined CSIR-National Chemical Laboratory (CSIR-NCL), Pune, in 2000 as a Scientist and rose to the level of Outstanding Scientist. He moved to IIT Palakkad in November 2024 and is currently serving as a Visiting Professor. He has been an elected fellow of the Indian Academy of Sciences since 2012. His research interests include heterogeneous catalysis, surface science under operando conditions, artificial photosynthesis, activation of small molecules and biomass components by photo/electro catalysis routes, and the development of novel multifunctional materials. He is also interested in taking the artificial photosynthesis process from the laboratory to the market.

aspect of this strategic approach is the elimination of the sluggish OER process.[4,5] Employing biomass-derived platform chemicals in photocatalysis, such as, glycerol, glucose, and 5-hydroxymethyl furfural (HMF), as oxidative reaction substrates is particularly appealing because both the charge carriers (e^- and h^+) employed are generated from sunlight absorption (SDG7-Affordable and clean energy and SDG-13-Climate action) and the organic feeds are renewable (SDG12-responsible consumption and production; and SDG-13), making the hydrogen production (SDG-13) process completely sustainable.[11] In addition, the VAPs resulting in the above-mentioned reaction is probably the most responsible way to generate them, without harming the environment in any manner (SDG-13). The energy efficient and environment friendly aspects of photocatalysis are not only utilized in water splitting, but also in other reactions, including the oxidation of biomass components,[5] CO_2 reduction to VAPs,[12] and oxidation of various contaminants during waste water treatments.[13]

The photocatalytic HER efficiency of the overall water splitting (OWS) reaction is critically limited by the sluggish four-electron OER process due to high overpotential, on the top of theoretical minimum of 1.23 V, and high possibility of electron–hole recombination.[5] In order to improve the photocatalytic HER efficiency, water splitting reactions are generally carried out with various hole scavengers such as simple alcohol, Na_2S + Na_2SO_3; though this approach enhances the HER, the energy of holes is wasted in unwanted oxidation to CO_2 *etc.* Employing biomass components such as glycerol and glucose provides an opportunity to utilize holes at a significantly lower potential than the OER as well as to produce VAPs.[14] Coupling H_2 production with biomass oxidation enhances the solar-to-fuel/chemical conversion efficiency as well as improves the rate of overall photoredox reactions.[5] Biomass components or derivatives such as glycerol,[5] benzyl alcohol, HMF, and glucose are generally employed for the co-production of H_2 and VAPs. Biomass component oxidation reactions are multi-step and more complex, but occur at a far lower potential, compared to the sluggish single-step OER; the former process involves the formation of C-based or O-based radicals (or charged species) and the cleavage of C–C/O–H/C–H bonds.[15] Electrocatalysis and photoelectrocatalysis methods are also employed for tandem utilization of redox efficiency of the materials to produce H_2 and VAPs *via* the reduction of water and the oxidation of biomass components.[16–19]

The novel aspect of coupling of water splitting to produce hydrogen and biomass oxidation to produce VAPs by concurrent utilization of photogenerated charge carriers is a rapidly evolving field. However, no comprehensive reviews are yet to be available in this field by covering a wide range of photocatalyst materials. In the current review, we critically analyze the recent advances in the field of photoredox reactions that involve water spitting and oxidation of biomass components. Finally, the challenges and perspectives of H_2 and VAPs generation *via* water splitting and biomass oxidation are also discussed. A Scopus-based survey was performed using different sets of key words to assess the evolution of photocatalytic coupled

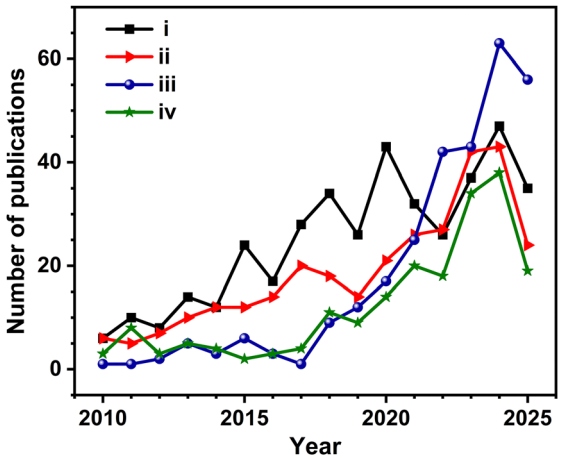

Fig. 1 Scopus-based survey (conducted on 14 July 2025) indicating the number of publications in the area of photocatalytic H_2 production coupled with the oxidation of different types of biomass components or biomass-derived materials using combinations of different sets of keywords, as follows: (i) photocatalytic or photocatalysis, glycerol (or glycerol reforming), and hydrogen. (ii) Photocatalytic or photocatalysis, glucose (or glucose reforming), and hydrogen. (iii) Photocatalytic or photocatalysis, benzyl alcohol (or benzyl alcohol reforming), and hydrogen. (iv) Photocatalytic or photocatalysis, biomass reforming, and hydrogen. Data for 2025 are up to July 14, 2025, and hence, they may be considered for 0.5 year.

reactions in the field of H_2 production and biomass oxidation reactions. The results of the survey suggest that single-digit numbers of papers were published between 2010 and 2015; however, a rapid increase in the number of publications for the last 10 years is evident (Fig. 1). Nonetheless, concurrent hydrogen production and biomass component oxidation to VAPs has

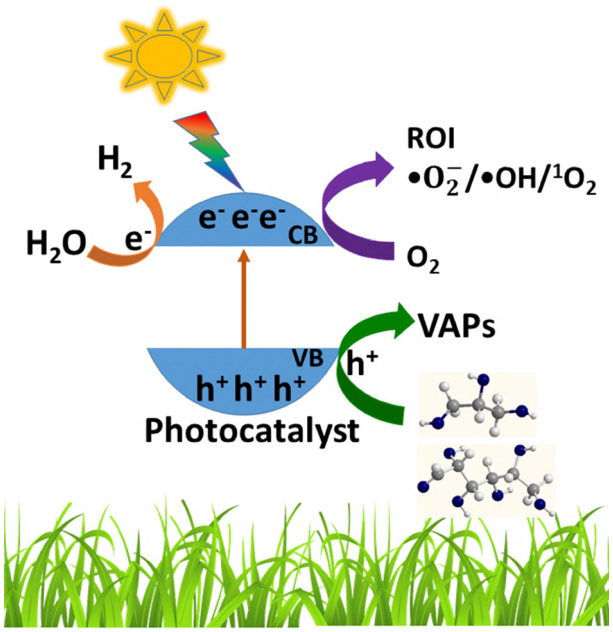

Fig. 2 Schematic of the conversion of biomass components to oxidized or reduced products using photocatalysts.

gained significant attention from 2020 onwards. Biomass-derived materials or biomass components have evolved as an important source of fuels, VAPs, and energy.

A schematic representation of biomass conversion to oxidized/reduced products *via* a photocatalysis approach is depicted in Fig. 2. The global annual production of biomass is over 170 billion metric tons.[20] If biomass components obtained from various sources could be properly utilized by a photocatalysis approach, significant amounts of fuels and VAPs can be generated, while tackling the disposal of biomass and addressing carbon-neutral economy simultanenously.[21] Fuels (methanol and ethanol) produced by the conversion of biomass have a great potential due to their drop-in fuel nature, and various VAPs offer several advantages.[22] This potential technique aligns with the idea of 'trash to treasure' together with the promotion of bio-circular economy with a closed carbon-cycle. Previous studies have revealed that a large number of photocatalysts have been utilized for the conversion of various types of biomass components under different reaction conditions.[1,23] Among the various photocatalysts, TiO_2-based systems have received much attention owing to their economically and environmentally benign properties and the ability to harvest and utilize sunlight.[14,24] The low conversion efficiency of biomass components is the main limitation of this process; however, pre-treatment of bio-mass components can resolve this issue to an extent.[25]

2. Heterojunctions in photoredox reactions

As several reviews are available for water splitting,[2,14,26–28] we suggest that readers refer to them for general aspects, such as various fundamental processes, band gap (E_g) engineering, role of co-catalysts and sacrificial agents, and efficiency aspects. The limiting factors of solar water splitting are addressed in our earlier review.[2] This review emphasizes the concurrent utilization of holes and electrons for generating oxidized VAPs from biomass components and hydrogen production from water reduction, respectively; critical aspects related to these processes are discussed throughout the review with relevant references. A semiconductor photocatalyst alone is not sufficient to carry out the photocatalysis reaction for several reasons, including light absorption from the limited wavelength region, absence of electron–hole pair separation at the interface, high charge recombination, and necessity of co-catalysts for redox reactions. Hence, it is invariably a light absorbing semiconductor combined with that of another semiconductor along with a co-catalyst, which could be any metal, metal oxide, *etc.* Although many semiconductors employed exhibit high extinction coefficient, the limited number of heterojunctions between semiconductors and co-catalysts hinder the electron–hole pair separation, which leads to poor utilization of charge carriers for redox reactions, and hence, low efficiency. Hence, a photocatalyst synthesis strategy should involve making the final photocatalyst with plenty of heterojunctions,[12] especially nanoscale heterojunctions between nanoparticles. Indeed, ref. 12 shows the number of nano-heterojunctions calculated to be between 174 trillion and 1 quadrillion in 1 mg of photoanode material between TiO_2 and $BiVO_4$, by selectively accommodating the quantum dots of latter in the nanopores of different sizes of the former by employing a SILAR synthesis method.

The formation of heterojunctions between two or more semiconductors at the nanoscale is advantageous for charge carrier separation and charge transfer processes. Based on the band structure, energy positions of the conduction band (CB) and valence band (VB), and the nature of photocatalyst semiconductors, heterojunctions have been classified into six types, namely type-I, type-II, type-III, p–n, Z-scheme and S-scheme heterojunctions; the schematics of all six heterojunctions are shown in Fig. 3. In the type-I (straddling gap) heterojunction, the CB and VB of photocatalyst B (PC B) with a smaller band-gap lies within a wide band gap photocatalyst A (PC-A). Both e^- and h^+ from PC A hop to PC B, resulting in the charge accumulation at the CB and VB of PC B. Charge accumulation leads to two drawbacks namely, the poor charge separation efficiency and low redox capability. Type-II (staggered gap) heterojunction is possible, when the CB and VB of one semiconductor photocatalyst (PC-A) lie above that of other photocatalysts (PC-B). Efficient charge transfer and e^-–h^+ separation occur in this type of heterojunction due to the transfer of electrons and holes in the opposite directions. It has more balanced and uniform distribution of charges in both components (PC-A and PC-B) with strong driving force-induced charge carrier separation, and many semiconductor combinations fall under this category.[5,12] However, it suffers from reduced redox potential and the same depends on the potential differences between PC-A and PC-B. In the case of type-III (broken gap) heterojunction, both the CB and the VB of PC-B lie below that of PC-A; hence, the dis-joined band positions of PC-A and PC-B limit the possibility of movement of charge carriers as well as separation between them.[29]

When a p-type semiconductor photocatalyst combined with that of n-type, a p–n heterojunction is formed between these two photocatalysts, and this is also a very commonly reported heterojunction. An internal inbuilt electric field (IEF) is created after the electron drift from the n-type semiconductor to the p-type semiconductor.[30] The IEF facilitates the charge transfer mechanism during photocatalysis, and the Fermi level (E_F) equilibration occurs at the heterojunctions under photocatalysis/illumination conditions. In Z-scheme heterojunctions, electrons in the CB of PC-B are transferred to the less positive VB of PC-A through the contact interface between the semiconductors.[31,32] This type of charge transfer process retains the electrons in more negative CB and the holes in more positive VB along with a decreased possibility of charge carrier recombination among them. Nevertheless, the recombination between electrons at the CB of PC-B and holes at the VB of PC-A (connected by blue arrows) cannot be eliminated, and hence, 50% of charge carriers are not effectively used for light harvesting purposes. It is also to be noted that natural photosynthesis adopts the Z-scheme, but in a complex manner, and

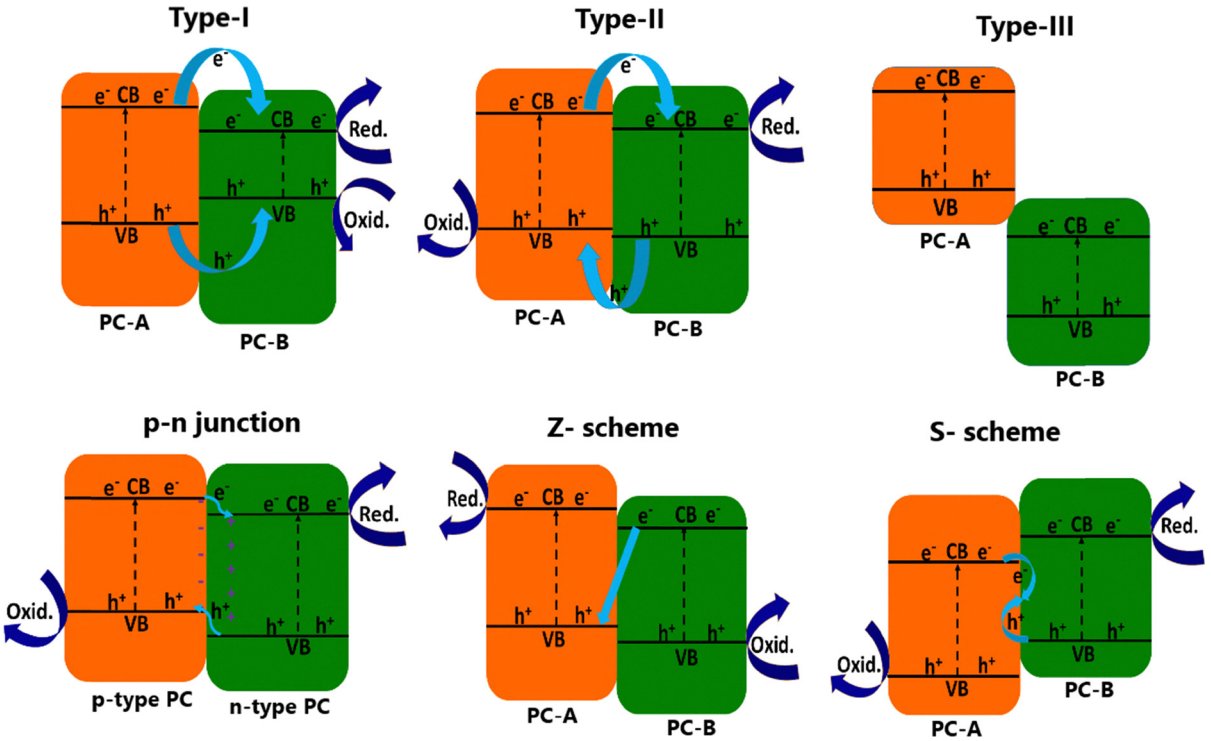

Fig. 3 Different types of heterojunctions formed between two different semiconductor photocatalysts. PC-A and PC-B refer to photocatalysts A and B, respectively.

utilizes electrons of the PS-II system to reduce $NADP^+$ to NADPH at PS-I; both PS-I and PS-II are connected by a pool of plastoquinones.[31a] The S-scheme or step-scheme heterojunctions are constructed between a highly oxidizing type of photocatalyst with highly positive VB and a high reduction type of photocatalyst with highly negative CB. Here charge transfer mode looks like an "S" shape after the inclusion of recombination path.[31b] In the S-scheme heterojunction, charge carriers with weak redox potentials undergo necessary recombination and get eliminated; hence, this step considerably reduced the energy loss. Charge carriers with strong redox potentials are retained, thereby maintaining a strong driving force and ensuring the photocatalyst system achieves high photoredox efficiency.

3. Important aspects of utilization of biomass components for oxidation

Heterogeneous photocatalysis for H_2 production has gained worldwide attention over the decades; however, the efficiency of this process is limited due to the sluggish OER and large extent of charge recombination. Due to these deficiencies, in spite of a large volume of work reported, it is yet to reach a decent technology readiness level (TRL). While the photochemical processes are adopted for commercial success, photocatalytic processes are yet to reach commercial success, due to the limitations such as low efficiency, low TRL, and use of costly sacrificial reagents. One critical reason is the overemphasis given to hydrogen production by water reduction, while holes are consumed by sacrificial agents to produce low-value or polluting molecules, such as CO_2. While light absorption and charge carrier generations are reported to be very good, the utilization of charge carriers for right redox reactions by minimizing charge recombination is the key towards improving TRL levels; this is yet to be achieved.

The aforementioned limitations could be addressed to a significant extent by using abundantly available biomass components such as glycerol and glucose as electron donors (by consuming holes). Foremost is the onset oxidation potential of biomass components ($\leq$1 V), which is significantly lower than that of water oxidation ($\geq$1.23 V) to O_2. For example, electrocatalytic glycerol oxidation has been recently reported[16,33,34] to occur at 0.4 V (*vs.* RHE) with Pd-nanocubes, while the same catalyst exhibits 1.5 V (*vs.* RHE) for the OER from water splitting. Low oxidation potential increases the possibility of employing many semiconductors with smaller bandgaps too, and hence, the materials scope increases significantly. The second important aspect is the observation of different products from glycerol oxidation, such as glyceric acid, 1,3-dihydroxyacetone (DHA), glycolaldehyde, and formic acid. This point underscores the step-wise or sequential oxidation of glycerol and intermediates to various products. Step-wise oxidation also underscores the effective utilization of holes through several steps, which is unlike a single-step OER process with four electrons. This aspect enhances the efficient utilization of holes generated in the light absorption process. It is to be noted that holes are minority charge carriers and their efficient

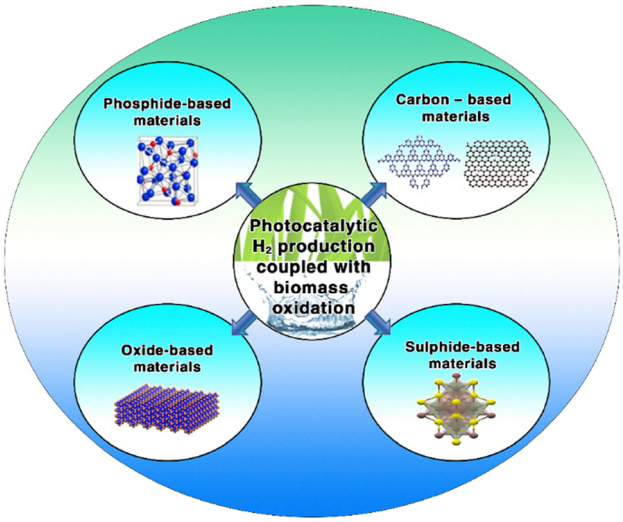

Fig. 4 Different types of photocatalysts employed in coupled photoredox reactions involving both H_2 production and biomass oxidation.

utilization enhances the electron utilization too for H_2 generation and, hence, an overall increase in kinetics. The third aspect is the selectivity of the oxidized products; a bandgap engineered photocatalyst with a precisely controlled VB energy can fine tune the product selectivity, as the product formation depends on the oxidation potential. Indeed, few works are reported with this aspect and much more work is necessary to increase the selectivity.

A wide variety of photocatalysts (Fig. 4) were employed as the bi-functional materials capable of producing H_2 and VAPs by parallel utilization of electrons and holes, respectively. Nonetheless, the development of a novel semiconductor photocatalyst system operating under sunlight and meeting the band position requirements for both the HER and the oxidation process is a challenge.[35] The band positions of widely used dual functional photocatalyst materials for the coupled production of H_2 and oxidation of biomass components are depicted in Fig. 5.

4. Metal oxide-based photocatalysts

Metal oxides (MOs) are one of the well-established front-liner materials in the field of photocatalysis owing to their inherent electrical and optical properties, as well as due to their sustainable nature in aqueous environements.[36] Among the MOs, semiconductor metal oxides have been at the forefront of photocatalysis for the past several decades. TiO_2 has been regarded as one of the flagship materials for photocatalytic applications since the pioneering work of Fujishima and Honda in 1972.[37] Titania (anatase phase) exhibits an E_g value around 3.2 eV; however, the wide E_g value of TiO_2 restricted its photocatalytic operations only under UV light.[38] Nonetheless, both CB and VB positions of titania are very much suitable for water splitting and the oxidation of most of the organic molecules such as glycerol, benzyl alcohol, and glucose.[39] The combination of TiO_2 with another visible light-absorbing photocatalyst, along with a co-catalyst, enhances the kinetics, and many examples are available in the literature.[5,10,40] Some of the important findings are reviewed in the first section under metal oxides.

4.1 TiO_2-based materials

Among the various photocatalysts, TiO_2-based heterogeneous photocatalysts have been established with various modifications over the past few decades; however, most of the previous works concentrated on water splitting with a sacrificial agent towards producing solar hydrogen.[38,41–45] In such reactions, holes are consumed by sacrificial agents mostly to minimize charge recombination, in order to increase the rate of HER. Only few literature reports are available that focus on exploiting holes as well as electrons to generate VAPs simultaneously.[5,46] Photocatalyst systems that can equally and efficiently handle both charge carriers for reduction and oxidation with high kinetics started appearing in the last few years, and in our opinion, they will be a boon to address the energy and environmental issues. For instance, Zhang *et al.* have investigated the simultaneous production of solar H_2 and oxidized products of cellulose, such as glucose, cellobiose, and formic acid from an

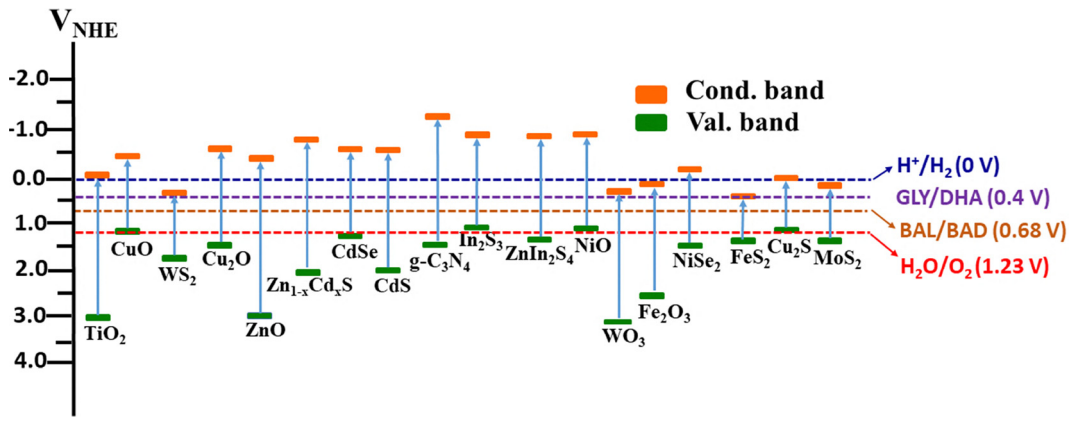

Fig. 5 Band positions of commonly employed photocatalysts at pH = 7. Some of the reference potentials are given for reader's reference. GLY/DHA indicates glycerol-to-dihydroxyacetone conversion; similarly, BAL/BAD represents benzyl alcohol-to-benzaldehyde conversion.

aqueous suspension of cellulose.[47] This approach gives new insights into the field of TiO_2-based heterogeneous photocatalysis.

Recent studies on biomass-component-based photocatalysis studies revealed the necessity of electronic integration of constituent components of photocatalysts for better utilization of electrons and holes.[5,10] Atom-like Cu-clusters are electronically integrated with TiO_2 and demonstrated to exhibit nearly half-a-quadrillion number of Schottky (Cu–TiO_2) junctions in 1 mg of photocatalyst; these junctions enhance the e^-–h^+ pair separation and the integration aspects allow the diffusion of charges to the surface redox sites. Cu–TiO_2 was employed by Bajpai *et al.* for simultaneous generation of VAPs and H_2 from the glycerol-water mixture.[10] The oxidation of glycerol was carried out in direct sunlight and this leads to C1, C2 and C3 oxygenates such as HCOOH, glycolaldehyde, DHA, and glyceraldehyde; high glycolaldehyde selectivity (75%) was reported. Photoredox efficiency of Cu–TiO_2 catalysts prepared *via* different methods, such as photo-deposition technique (TC-PD), borohydride-treated TiO_2 followed by Cu-deposition (in dark) (TC-200), and deposition *via* UV illumination-induced oxygen-vacancy creation followed by Cu^{2+}-to-Cu reduction (in dark) (TC-PDO), are compared. It is to be noted that a pale blue colour reported with the latter two procedures, after the first step of borohydride treatment or UV-illumination, directly hints the availability of oxygen vacancies and Ti^{3+} sites. While the direct photodeposition could possibly increase the Cu-cluster size, the latter two procedures would be selectively depositing Cu atoms or atom-like Cu-clusters at the free electron(s) sites, which are also dispersed, on the host TiO_2. Interestingly, TC-PDO exhibited the highest solar H_2 yield (5.1 mmol g^{-1} h^{-1}), which are 200 and 130% that of TC-200 and TC-PD, respectively. The highest Cu-distribution observed on TC-PDO underscores and correlates well with that of the highest H_2 yield observed; this indeed underscores the efficient charge separation and electron utilization. The effect of pH on the photoredox performance of the TC-PDO catalyst was also evaluated; the results indicated that compared to the neutral medium (pH = 7), the HER rate and liquid VAP formation rates were increased in the alkaline medium (pH = 9) by 2.5 times. It is well known that a higher pH shifts the VB and CB to a less negative energy, which is known to favor H_2 production. The alkaline medium is also known to facilitate the C–C cleavage, and hence, overall, it is highly beneficial for the conversion of glycerol and water splitting. A sustainable activity observed for 25 h suggested that TC-PDO Cu–TiO_2 catalyst system could be evaluated for large scale studies.

In a similar study by Bajpai *et al.*, but with anionic-Au integrated with P25–TiO_2 ($Au^{\delta-}$@TiO_2), three liquid products, namely DHA, glycolaldehyde and formic acid along with parallel H_2 production, were observed from aqueous glycerol *via* photoredox catalysis.[40] A maximum glycerol conversion of 13% with 52 and 23% selectivity for glycolaldehyde and DHA, respectively, was obtained under anaerobic conditions in 5 h. A comparison of the photocatalytic activity under aerobic and anaerobic conditions revealed that the highest product yield was achieved under aerobic conditions (Fig. 6a and b). An excellent photoredox activity and effective separation of photogenerated charge carriers by $Au^{\delta-}$@TiO_2 were attributed to the uniform distribution of Au on TiO_2, and the strong electronic integration as well as the formation of nano-Schottky junctions between Au and TiO_2. The existence of anionic-Au acts as the electron sink and reduces the protons to H_2, while holes present at the VB of TiO_2 oxidize glycerol to DHA, glycolaldehyde and formic acid (Fig. 6c). Anaerobic conditions show a H_2 yield which is more than an order of magnitude higher than that with aerobic conditions, which underscores the utilization of electrons for the conversion of molecular oxygen to reactive intermediate species for glycerol oxidation. Aerobic condition also leads to a CO_2 yield 3 times higher than that of anaerobic conditions. This provides an opportunity to fine-tune the reaction conditions with the required amount of oxygen to move towards the desired product with no over-oxidation to CO_2. The formation of formic acid is a clear indication of hole-driven C–C cleavage of glycerol during oxidation. Ref. 10 and 40 deal with Cu@TiO_2 and $Au^{\delta-}$@TiO_2, respectively, exhibiting similar product patterns but with significantly different activities and selectivities, which is interesting; indeed, the latter shows that the high commercial value of DHA with higher selectivity is worth noting.

A biochar-supported CdS/TiO_2 photocatalyst (CdS/TiO_2/BC) exhibited co-production of H_2 and organic acids through photoreforming of glucose.[48] The selectivity of organic acids, obtained through the photoreforming of glucose, was modulated by employing different types of bases. In the presence of 25 mM NaOH, H_2 production ($\sim$12.77 mmol g^{-1} h^{-1}) was obtained with acetic acid (selectivity of 63.94%). It is also necessary to add alkali periodically to maintain high pH and activity, due to the neutralization of acetic acid by alkali. While in the presence of 3 mM Na_2CO_3, formic acid was formed (selectivity of 60.29%) along with H_2 ($\sim$10.29 mmol g^{-1} h^{-1}). Trapping tests confirmed that $^{\bullet}O_2^-$ and $^{\bullet}$OH were responsible for the activation of glucose and the formation of acetic acid.

A series of NiO–TiO_2 photocatalysts with p–n heterojunctions were demonstrated to produce H_2, glyceraldehyde and DHA with 20% glycerol conversion.[49] The yield of glyceraldehyde was higher than that of DHA up to 22 h of reaction; however, after 24 h, the yield of both glyceraldehyde and DHA became almost equal. The photogenerated electrons and holes were accumulated on TiO_2 and NiO, respectively. Hence, photocatalytic reduction and oxidation occur on the surface of TiO_2 and NiO, respectively. A techno economic analysis (TEA) was performed to evaluate the performance of the catalyst system and economic viability of the photocatalytic process. The major capital expenditure (CAPEX) costs were related to the solar farm, and the highest contributor to the annual operating expenditure (OPEX) was the annual cost required for the replacement of the catalyst. The annual revenue obtained by the liquid and gaseous products including glyceraldehyde, DHA and H_2 was 89, 11 and 0.03%, respectively. TEA presented in ref. 49 and a recent review on enhancement in the rate of photocatalysis[2] in direct sunlight in panel forms are worth

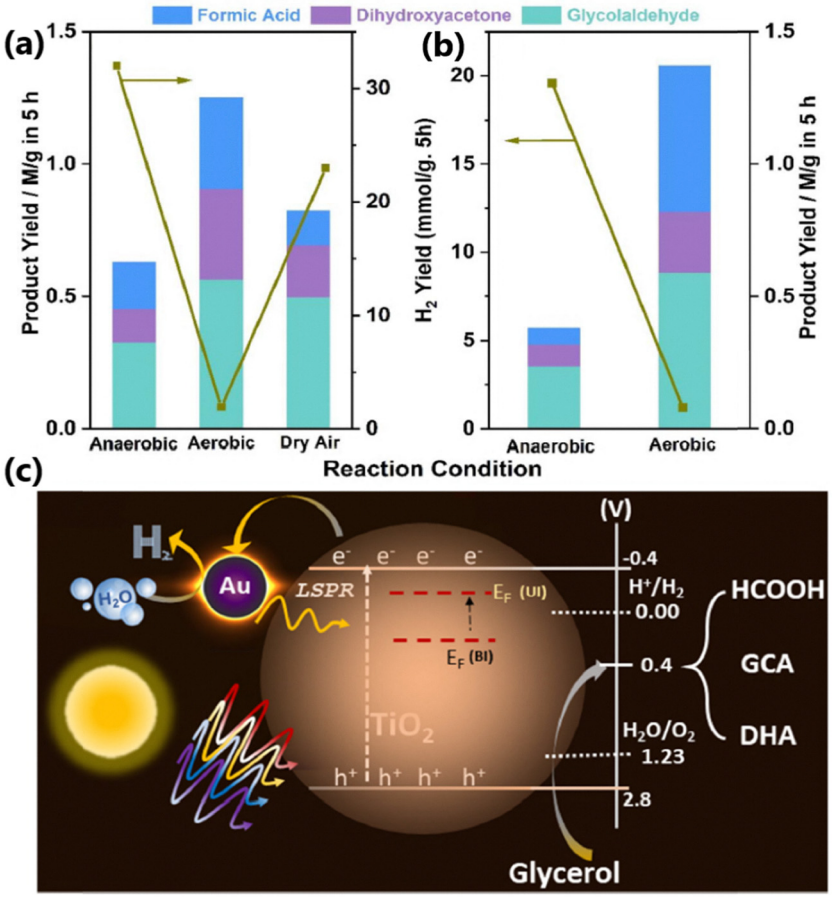

Fig. 6 Photocatalytic glycerol oxidation with 0.5% Au@TiO_2 under (a) direct sunlight with an average intensity of 60 mW cm^{-2} and (b) one sun condition with an AM 1.5 filter (100 mW cm^{-2}). All product concentrations were for five hours of the reaction time in both panels. (c) Possible mechanism for plasmon-induced Au@TiO_2 toward photocatalytic hydrogen generation and glycerol oxidation towards value-added products. E_F levels shown are indicative and not to the scale; however, an upward shift under illumination occurs due to electron storage in gold clusters. Abbreviations: E_F (UI), Fermi level under illumination; E_F (BI), Fermi level before illumination or a fresh catalyst; GCA, glycolaldehyde; and DHA, dihydroxyacetone.[40] Reproduced with permission. Copyright 2024, the Royal Society of Chemistry (RSC).

comparing. Later review highlights a great enhancement in the activity of photocatalysts deposited in panel forms with a minimum amount of catalyst (1 mg cm^{-2}), due to efficient solar harvesting of sunlight along with other reasons. With recycling of the reactant solution by a continuous flow process, glycerol conversion can also be enhanced to higher levels than those reported in ref. 49.

A ternary $RuP_2/Ti_4P_6O_{23}$@TiO_2-7 photocatalyst consisting of *in situ* introduced RuP_2 and $Ti_4P_6O_{23}$ on the surface of TiO_2 is identified as a potential photocatalyst, which produces H_2 (16.3 mmol g^{-1} h^{-1}) and lactic acid (2.41 mmol g^{-1} h^{-1}) from water and arabinose in an alkaline medium (0.1 to 5 mol per L KOH) with high stability over 5 cycles.[50] The presence of uniformly arranged nanospherical particles of $RuP_2/Ti_4P_6O_{23}$@-TiO_2-7 not only significantly increases the number of active sites but also facilitates the swift diffusion of photogenerated charge carriers. The incorporation of RuP_2 and $Ti_4P_6O_{23}$ leads to the formation of a heterojunction as well as providing a large number of edge active sites for the HER. The redox photocatalytic efficiency of the catalyst system has been successfully tested in the aqueous solution of monosaccharides and macromolecule xylan. It was found that $RuP_2/Ti_4P_6O_{23}$@TiO_2-7 converted pentose sugars efficiently to lactic acid than that of hexoses. For xylan, lactic acid and H_2 production reached up to 0.63 gg_{xylan}^{-1} and 0.6 mmol g^{-1} h^{-1}, respectively, along with the production of formic acid and acetic acid. EPR studies revealed that $^1O_2$, $^\bullet O_2^-$, h^+, and $^\bullet$OH species were responsible for the generation of lactic acid, in which $^\bullet$OH radicals produced by the reaction between h^+ and OH^- play a crucial role in the oxidation of biomass-derived sugar molecules.

Charge carrier diffusion effect, driven by the difference in carrier concentration, caused the transfer of photogenerated electrons in the opposite direction of the IEF constructed between CuS and TiO_2, thereby facilitating the formation of *N*-benzylidenebenzylamine and H_2 production.[51] In fact, Z-scheme heterojunctions play a vital role in the transfer of photogenerated electrons and holes to reduction and oxidation sites for water reduction and benzylamine oxidation, respectively. Electrons enriched in the CB of CuS reduce water to H_2, while the holes present at the VB of TiO_2 oxidize water to $^\bullet$OH

or $^{-}$OH. Subsequently, the $^{\bullet}$OH radical oxidizes benzylamine to C-centered α-amine radicals ($C_6H_5CH_2NH_2^{\bullet+}$). In the next stage, $C_6H_5CH_2NH_2^{\bullet+}$ radicals undergo a H^+-transfer reaction to form C_6H_5CHNH, which coupled with another benzylamine molecule to form *N*-benzylidenebenzylamine (selectivity >99%).

Selective formation and preservation of formic acid, by the oxidation of cellulose resources, are perplexing. However, You *et al.* have successfully preserved formic acid during the oxidation of cellulose in an aqueous medium with ZnSe/Pt@TiO_2.[52] Oxygen vacancies formed at the surface of TiO_2 preserve formic acid as the final liquid product, even after 140 h of reaction. The photocatalyst h-ZnSe/Pt@TiO_2 produced 14 386, 11 655, 12 855, and 12 156 μmol g^{-1} h^{-1} of H_2 and 372, 234, 251, and 248 μmol g^{-1} h^{-1} of formic acid with ball-milled α-cellulose, wood, paper, and grass as the substrates, respectively. Cellulose molecules were degraded to polyhydroxy species, namely, glucose and glycidaldehyde; these polyhydroxy species were preferably adsorbed on oxygen vacancy-enriched TiO_2 and undergo oxidation by holes. The Pt-cocatalyst deposited on ZnSe shortens the path for the HER, and oxygen vacancies on the TiO_2 surface reduce the transfer path of the holes from the photocatalyst surface to the substrates. As glucose is more soluble in water, it was used for analyzing the oxidation process. Reforming of glucose proceeded *via* its oxidation to gluconic acid and then to pentose by eliminating a molecule of formic acid. Pentose undergoes degradation to tetrose and then to trihydroxy-butanoic acid by eliminating another molecule of formic acid. This process of elimination of formic acid is repeated until the reaction medium left only with formic acid. Even though the formic acid is preserved up to an extent, its further oxidation to CO_2 was also observed. Periodic removal of formic acid from the reaction medium is one of the possible solutions to address this issue.

Nivedhitha *et al.* reported concurrent H_2 production and glycerol oxidation over visible light-absorbing mixed metal phosphate $(Ni/Co)_3(PO_4)_2$ (CoNiP) integrated with commercial P25–TiO_2.[5] The photocatalyst TiO_2–CoNiP X : Y (contains 1 wt% CoNiP on TiO_2) is composed of bimetal (Co and Ni) phosphates with different Co/Ni ratios such as 10/0, 7/3, 5/5, 3/7, and 0/10. The best performing catalyst, containing 1 : 1 (5 : 5) composition of CoNiP (TiO_2–CoNiP-5 : 5) on TiO_2, has generated 54 and 67 mmol g^{-1} 25 h^{-1} H_2 and glyceric acid (with 85% selectivity), respectively, under one sun conditions. One sun condition refers to the standard solar irradiance with 100 mW cm^{-2} power density with an AM 1.5G filter. The enhanced photoredox performance of TiO_2–CoNiP was attributed to the p–n heterojunction between TiO_2 and CoNiP and the uniform distribution of CoNiP on the surface of TiO_2. Parallel utilization of photogenerated electrons and holes is beneficial for the green and sustainable aspects of photoredox reactions. A higher concentration of overall oxidized products compared to H_2 production is indicating the better utilization of holes. A lower HER rate suggests the possible formation of reactive oxygen species (ROS) and the reduction of some organic molecules formed during the intermediate step of oxidation mechanism. These observations hint the necessity of incorporating *in situ* studies or conducting separate experiments to identify the reaction intermediate during the oxidation reactions. Such studies will help to improve the selectivity of oxidized products and also to enhance the overall utilization of electrons and holes by eliminating the unwanted side reactions. Such studies also show a higher utilization of holes for the oxidation with organic molecules than the OER of overall water splitting. While oxygen has a very low commercial value, VAPs such as glyceric acid have a high commercial value. Apart from this, four-electron processes involved in glycerol-to-glyceric acid conversion would correspondingly generate two hydrogen molecules. A simple molecular weight comparison of $2H_2$ (4 g) and glyceric acid (106 g) underscores the value addition in the entire process. For every kilogram of H_2, 26.5 kg of glyceric acid would be produced. It is one of the expensive chemicals and its enantiomers have a high pharmaceutical value.

Salgaonkar *et al.* demonstrated that the photocatalytic conversion of butanols (*n*-butanol, iso-butanol and 2-butanol) to butanal/butanone together with the production of H_2 was obtained by using a thin-film form of TiO_2-based catalyst loaded with Pd nanoparticles with different morphologies (Pd-polycrystalline (Pd_{PC}), Pd-nanocube (Pd_{NC}), and Pd-truncated octahedron (Pd_{TO})) and their counterparts with half-a-monolayer Pt coated on Pd ($0.5\theta_{Pt}$ − Pd) under one sun condition with an AM 1.5 filter.[53] Among the butanols, the highest conversion was achieved with 2-butanol compared to isobutanol and *n*-butanol. The catalyst loaded with 1 wt% of cocatalyst ($0.5\theta_{Pt}$ − Pd_{TO}/TiO_2) exhibited the highest conversion of 2-butanol to butanone (13.6%) with an H_2 production rate of 16.2 μmol mg^{-1} in 4 h under one sun condition. Further, the reactions carried out under aerobic and anaerobic conditions show that the butanol oxidation was increased, and H_2 production decreased under aerobic conditions. The enhanced photocatalytic performance of $0.5\theta_{Pt}$ − Pd_{TO}/TiO_2 compared to virgin TiO_2 is attributed to the efficient e^-–h^+ separation achieved through the electron trapping by Pt-coated Pd.

In a different work, thin film form of *in situ* generated Ti^{3+} on TiO_2 with finely dispersed NiO photocatalyst, namely, NiO/Ti^{3+}–TiO_2 nanocomposite (NiT-*n*, where *n* = 1–4 indicates increasing mol% of Ni from 1 to 4), was used for simultaneous utilization of charge carriers to generate H_2 and VAPs, such as, DHA, glycolaldehyde, and formic acid, through synchronized water spitting and glycerol oxidation.[30] The *in situ* generation of Ti^{3+} is achieved by a modified sol–gel method without using any reducing agents (Fig. 7a). The best performing catalyst (NiT-3) generated 15.62 mmol h^{-1} g^{-1} of H_2 and 2.29 mmol h^{-1} g^{-1} of oxidized products with 51.1% selectivity towards glycolaldehyde under anaerobic conditions. It was reported that solar H_2 formation occurs at the CB of TiO_2, while the highly efficient holes present in the VB of TiO_2 and NiO could oxidize glycerol molecules and also cleaved the C–C bonds of glycerol to produce C_1, C_2 and C_3 products. However, the photoredox efficiency under aerobic conditions revealed that a significant number of electrons were used for the formation of ROS, namely superoxide and peroxides; this, in turn, facilitates the oxidation process and increases the oxidized product yield to

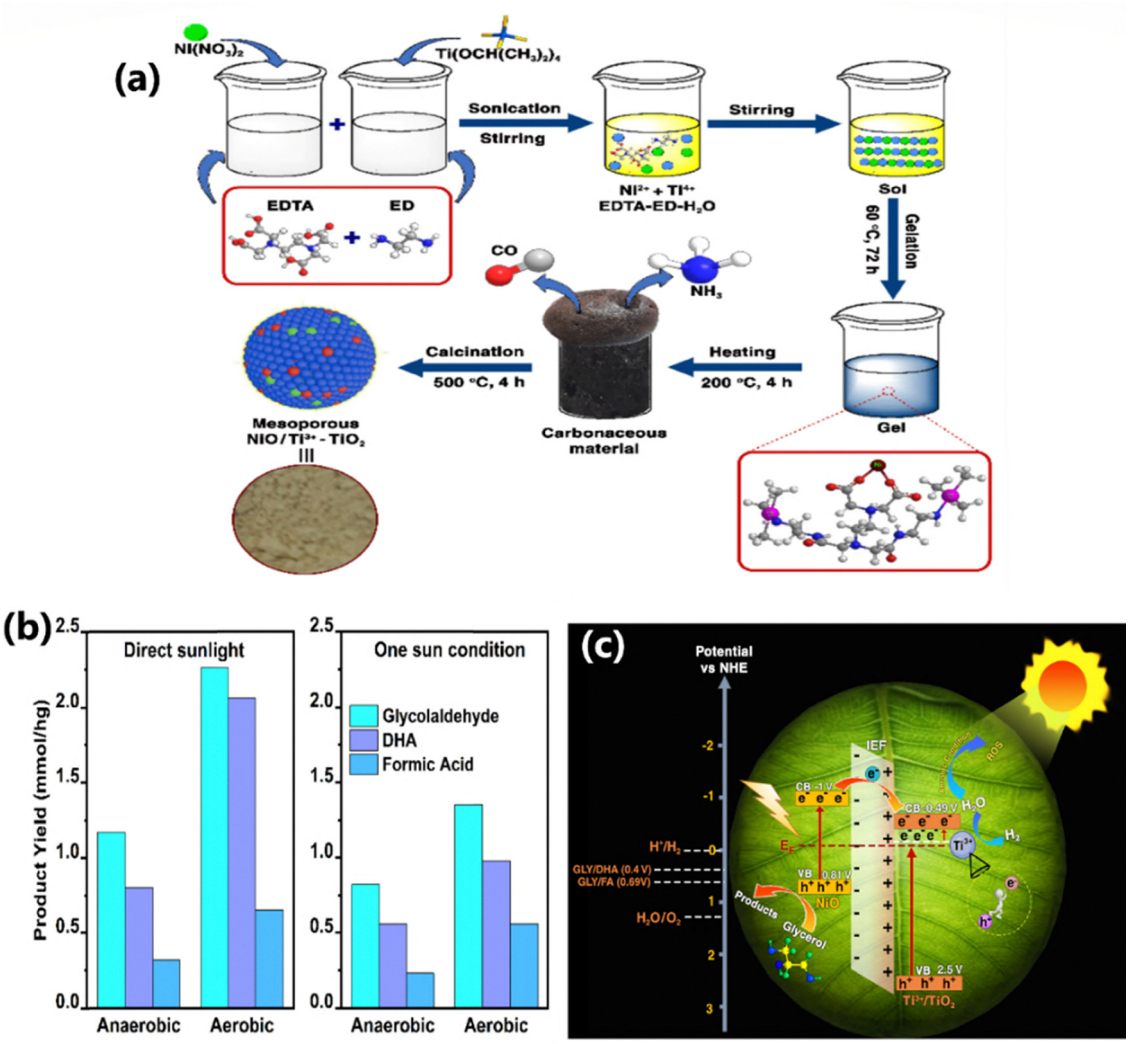

Fig. 7 (a) Schematic of the sequential steps involved in the synthesis of mesoporous NiO/Ti^{3+}–TiO_2 nanocomposite. (b) Product yield of photocatalytic glycerol oxidation on NiT-3 under direct sunlight illumination and one sun condition (100 mW cm^{-2}) in anaerobic and aerobic conditions. (c) Schematic of a possible mechanism for NiO/Ti^{3+}–TiO_2 towards photocatalytic hydrogen generation under direct sunlight.[30] Reproduced with permission. Copyright 2025, RSC.

4.9 mmol h^{-1} g^{-1} (Fig. 7b), twice that of anaerobic conditions. It causes the deficiency of electrons for water splitting, and as a result, the H_2 yield diminishes. However, under anaerobic conditions, very less ROS were formed, electrons are utilized to the maximum extent for the reduction of protons from water and holes are only involved in the oxidation of glycerol. In addition, experiments in direct sunlight appear to give higher product yields, than one sun conditions (with an AM 1.5 filter) carried out under ambient temperatures. The enhanced photoredox efficiency of NiO/Ti^{3+}–TiO_2 nanocomposites was attributed to the presence of the mid-gap or local states formed by Ti^{3+} and the formation of p–n heterojunctions between NiO and Ti^{3+}–TiO_2, and IEF drives the charge carrier transfer process. Interestingly, the VB edge of NiT-*x* shifts to lower negative values between 0.6 and 0.9 eV, compared to TiO_2, underscoring the Ni-doping into the lattice of the latter, resulting in an electronic integration. The oxidation of glycerol occurs at the VB of NiO as well as Ti^{3+}–TiO_2, since their VB potential is higher than the glycerol oxidation potential. However, electrons in the CB of TiO_2 reduce water to H_2 (Fig. 7c), with electron transfer from the CB of NiO to TiO_2.

Dual functional properties, especially highly selective oxidation and the efficiency to convert benzyl alcohol to benzaldehyde (BAD) using TiO_2 nanoparticles, were improved by the integration of sulfur vacancy-rich ZnS nanowires.[54] The photoredox reactions involving electrons and holes for water splitting and benzyl alcohol oxidation, respectively, led to the production of 15.23 mmol g^{-1} of H_2 and a BAD yield of 88.5% after 5 h of reaction. Even though the ZnS/TiO_2 heterostructure produced H_2 and O_2 from pure water, the amount of H_2 was very low compared to that of benzyl alcohol–water.

Concurrent methanol oxidation to formaldehyde and water splitting to H_2 was demonstrated by Nalajala *et al.* with different morphologies of Pd nanoparticles (Pd_{PC}-polycrystalline;

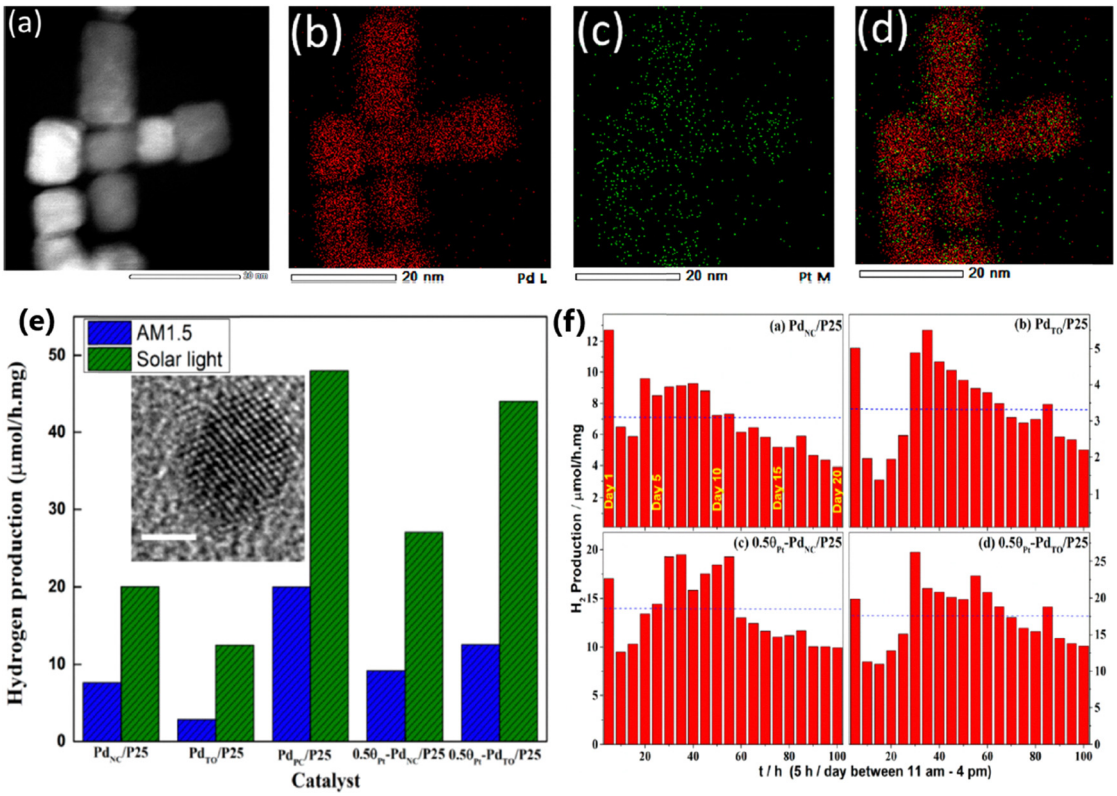

Fig. 8 (a) STEM image of 0.5θ_{Pt} – Pd$_{NC}$, corresponding elemental distribution of (b) Pd (red) and (c) Pt (green), and an overlay of (d) Pt and Pd. Very sparse distribution of Pt on Pd fully supports the half-a-monolayer surface coverage of Pt on Pd. (e) Hydrogen production activity of thin films of prepared catalysts using aqueous methanol under one sun and direct sun light conditions. Inset: HRTEM image of the Pd$_{PC}$ single particle at a scale of 2 nm. (f) Time-dependent H_2 generation activity for all photocatalysts under direct sunlight. The median value of hydrogen production is given as a dashed blue line in the respective panels.[55] Reproduced with permission. Copyright 2021, the American Chemical Society (ACS).

Pd$_{NC}$-nanocube; Pd$_{TO}$-truncated octahedron) prepared and anchored on TiO_2.[55] In addition, half-a-monolayer of Pt was coated on Pd$_{NC}$ and Pd$_{TO}$ and anchored on TiO_2 and evaluated for the same reaction. Fig. 8a–d show the exclusive coating of Pt on the surface of Pd$_{NC}$ and the STEM results nicely capture the same. At the outset, this paper may appear to describe sacrificial-agent-assisted water splitting; however, this is not the case. No CO or CO_2 was observed in this particular reaction, rather formaldehyde formation was detected. Especially, catalysts coated in a thin-film form were demonstrated to show an order of magnitude higher activity than that of its powder counterpart measured in a suspension. For example, Pd$_{NC}$/P25 shows 7.6 and 0.5 μmol h^{-1} mg^{-1} solar H_2 generation under one sun illumination with an AM 1.5 filter. This highlights the necessity to estimate the activity in different forms of catalysts to know the intrinsic activity, and the thin film appears to be one of the better methods to adopt. A comparison of solar hydrogen generation activity shown in Fig. 8e for different Pd/P25 catalysts demonstrates the highest activity with Pd$_{PC}$/P25 in direct sunlight. Catalysts were also subjected to concurrent oxidation and reduction of methanol and water to formaldehyde and H_2, respectively. Experiments carried out for 20 days continuously under direct sunlight show the robust and sustainable nature of the catalyst for experimental conditions (Fig. 8f). Pd$_{PC}$/P25 is reported to generate 48 μmol h^{-1} mg^{-1} solar H_2 and 0.3 μmol h^{-1} mg^{-1} formaldehyde in direct sunlight. Indeed, this result also indicates better utilization of electrons for H_2, rather than formaldehyde formation, and it appears that there is scope to improve the performance by varying the experimental conditions. In addition, the temperature measured under direct sunlight for photocatalysis was reported to be around 55 ± 5 °C, and this factor leads to 2–3 times enhancement in activity than those experiments carried out under one sun illumination. This fact underscores the utilization of thermal effects for the reaction to improve the kinetics, in direct sunlight.

A $BiVO_4$–TiO_2 (BVT) photoanode was prepared by selectively accommodating $BiVO_4$ QDs within the nano-pores of commercial P25–TiO_2 *via* the SILAR method and employed for the selective oxidation of glycerol; just by varying the glycerol content, lactic acid or glyceric acid was selectively produced along with parallel production of H_2 from water.[56] The HRTEM images of the BVT photoanode material (Fig. 9a–d) indicating the $BiVO_4$ particles are uniformly filled within the micro- and meso-pores of TiO_2. The BVT photoanode was employed with Pt as the co-catalyst, and it was found that a simple change in concentration of glycerol, from 1 to 100 mM, has significantly changed the selectivity of liquid products (Fig. 9e and f). At a

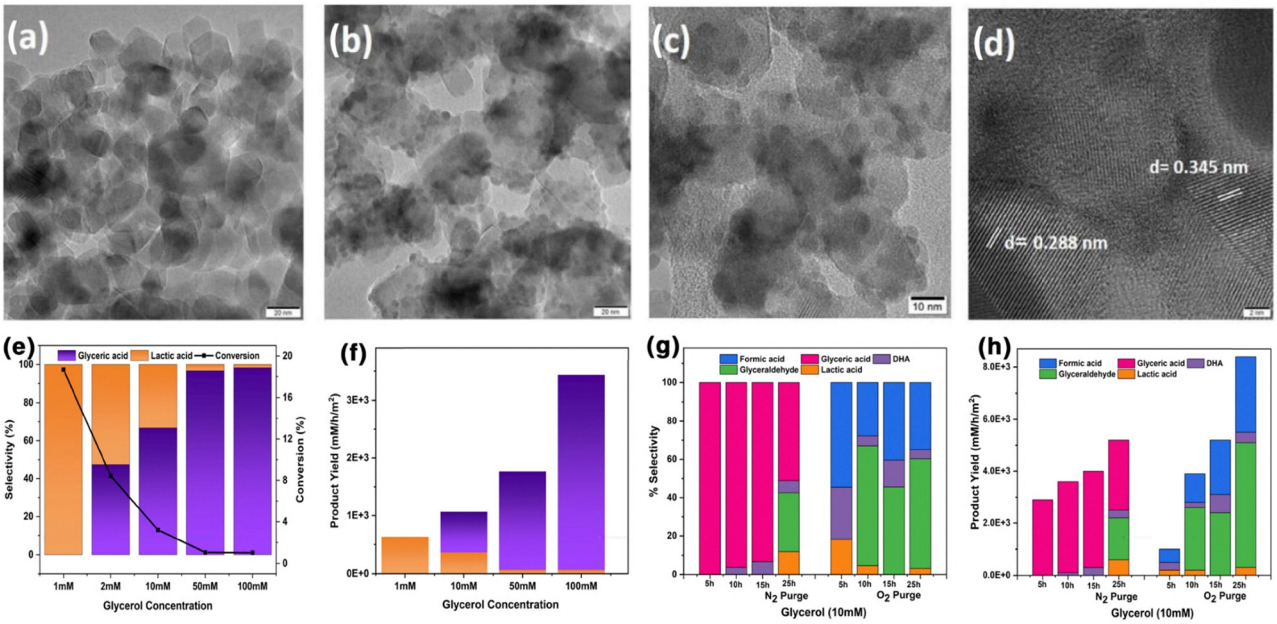

Fig. 9 HRTEM images of (a) TiO_2 (scale bar 20 nm) and (b)–(d) the BVT photoanode at various magnifications with scale bars of 20 nm, 10 nm, and 2 nm, respectively. (e) Product selectivity and glycerol conversion and (f) product yield after photocatalytic glycerol oxidation at different concentrations of glycerol under one sun condition with BVT-Pt. All the results shown are after 3 h of continuous reaction. (g) Product selectivity (left panel) and h) product yield (right panel) after photocatalytic glycerol oxidation (10 mM glycerol concentration) with N_2 purging and O_2 purging under one sun condition as a function of reaction time.[56] Reproduced with permission. Copyright 2025, Wiley.

lower concentration of glycerol (1 mM), the major product was lactic acid (100% selectivity), while at a higher concentration (100 mM), glyceric acid was the major product (98%) with a minor concentration of lactic acid. With the increase in glycerol content in the reaction mixture, the glyceric acid selectivity increases. This study further explores the impact of different reaction environments (aerobic and anaerobic) over a longer period of time on the yield and selectivity of oxidized products (Fig. 9g and h). It shows that under anaerobic conditions, only glyceric acid was produced in a short period of reaction time; however, on prolonging the reaction to longer hours (25 h), other C3-oxygenates were also produced (glyceric acid, DHA, lactic acid and glyceraldehyde). However, under aerobic conditions, three different products, namely, lactic acid, DHA and formic acid were generated within a short time, with high formic acid selectivity. After 25 h of reaction, a small amount of lactic acid was also observed with high glyceraldehyde selectivity. These observations demonstrate that BVT selectively produces a single product under anaerobic conditions, while an increased number of products were obtained with less selectivity under aerobic conditions. Even though simultaneous H_2 production was observed with BVT, a low yield indicates the possibility of secondary reactions to form ROS by the consumption of electrons. Nonetheless, this study paves the way to tune the selectivity of the product by varying the reaction conditions, such as N_2 or O_2 or a mixture of N_2 + O_2, initial glycerol concentration, and reaction time, and it is worth exploring further. Recent femtosecond transient absorption spectroscopy experiments carried out with BVT[56] to explore the excited state dynamics demonstrated the availability of long-lived charge carriers ($\gg$6 ns), due to the large minimization of recombination, which is due to the abundantly available heterojunctions. This study also shows new trap states evolved under illumination conditions, which are long-lived and hinder charge recombination. Although BVT exhibits an E_g value around 2.5 eV, transient absorption measurements demonstrate a strong positive band in the mid-visible wavelength range due to intra-band transitions. The formation of heterojunctions results in the formation of newer states that absorb well in the mid-visible regions; 7% IPCE (incident photon to current efficiency) performance observed between 520 and 700 nm substantiates the above claim.

4.2. Other oxide-based materials

The coupled effect of Z-scheme heterojunctions and localized surface plasmon resonance (LSPR) effect, induced by monoclinic tungsten oxide ($W_{18}O_{49}$), to sensitize $ZnIn_2S_4$ was utilized for absorption from the entire visible range photons for photoredox reactions.[57] Nearly comparable H_2 and BAD yields were obtained with the optimal catalyst, indicating the equal participation of electrons and holes with a utilization efficiency equal to one. The excess heat dissipated as a result of the non-radiative recombination of hot e^- and h^+ creates a photothermal effect in the catalyst, which, in turn, accelerates the photocatalytic reaction kinetics. Moreover, the hybrid catalyst system demonstrated a solar-to-hydrogen (STH) conversion efficiency of 0.466% and a solar-to-chemical (STC) conversion efficiency of 0.024%. The results from *in situ* EPR measurements (Fig. 10a–c) show that electrons and holes were involved in the reduction and oxidation of water and benzyl alcohol,

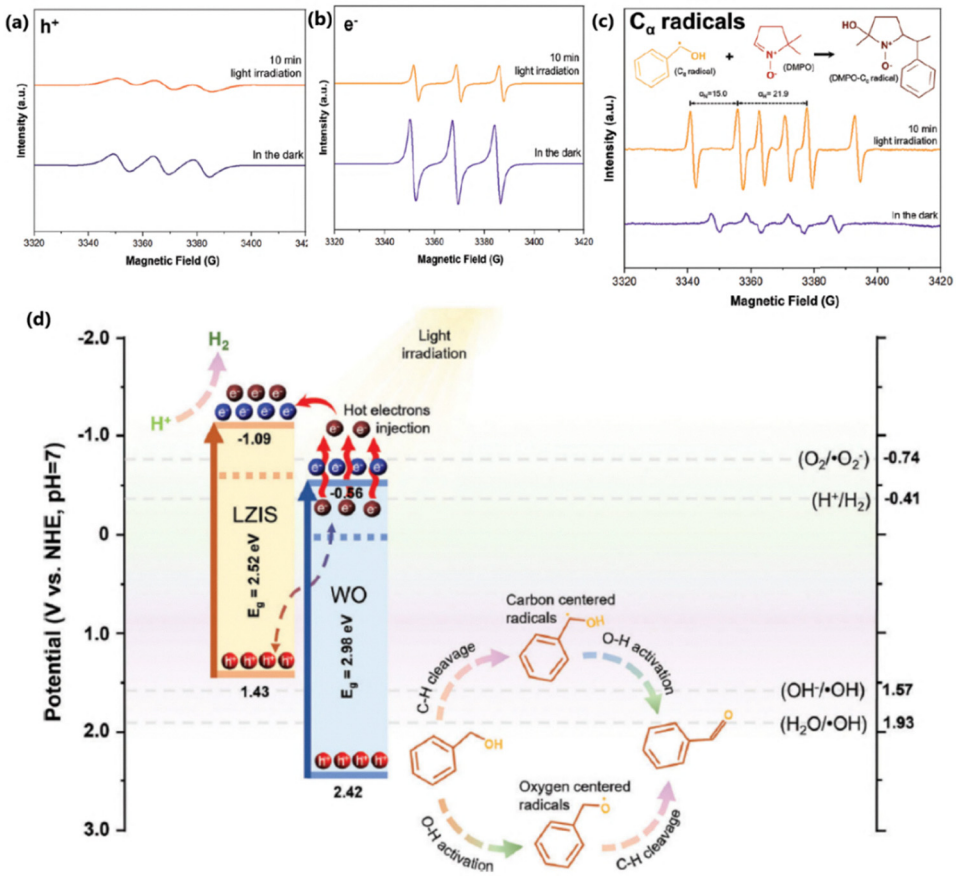

Fig. 10 EPR spectra of (a) holes and (b) electrons in the presence of TEMPO and (c) EPR spectra of DMPO-α-hydroxybenzyl radicals under dark and light illumination. (d) Postulated band position and mechanistic insight into photoredox H_2 production coupled with BA oxidation over the optimal 50ZW.[57] Reproduced with permission. Copyright 2024, Wiley.

respectively, with the formation of free radical species. The oxidation of benzyl alcohol follows two pathways: the first one involves oxygen-centered benzyloxy radicals, and the other by carbon-centered hydroxybenzyl radicals. The benzyloxy radicals subsequently yield BAD by a dehydrogenation process, while the holes react with hydroxybenzyl radicals to form BAD. The involvement of holes in the oxidation of benzyl alcohol suppresses the formation of non-selective radical species such as •OH, leading to the selective formation of BAD. However, dehydrogenated protons from benzyl alcohol and water are reduced to H_2 at the CB of $ZnIn_2S_4$ (see Fig. 10d).

Machine learning (ML)-assisted studies have been carried out recently[58] on the conversion of glycerol, which revealed that co-catalysts play a crucial role, especially in the formation of intermediate products. As indicated earlier in many studies,[5,10,40,56] various process involved, such as selective activation of C–H bonds, C–C bond cleavage, C–O (and C=O) bond formation, were dependent on the co-catalyst employed. For example, the Rh co-catalyst exhibits a better C–C bond cleavage efficiency than the Ag co-catalyst; however, Ag shows a better activity towards the formation of C–O bonds. Analysis of the impact of various co-catalysts on E_g and HER rates revealed that Pt, Ag and Fe exhibit low E_g, whereas Pt, $NiSe_2$ and La show better HER efficiency. Dataset analysis further revealed that Pt is the most commonly used co-catalyst along with Pd, Au and Ag, suggesting their supremacy in photocatalytic efficiency irrespective of their high cost. Nonetheless, Co/Ni–phosphate[5] exhibited the highest (85%) glyceric acid selectivity in glycerol conversion; there are few other systems available with different co-catalysts with high selectivity. In addition, the highly complex nature of biomass component oxidation under photocatalysis conditions demands a more rigorous ML analysis to understand the role of various factors and to what extent they influence the final outcome of the reaction.

5. Chalcogenide (sulfur)-based photocatalysts

Metal chalcogenides have received wide attention in photocatalysis due to their narrow E_g and high extinction coefficient.[59] Based on the number of elements present, they are broadly classified as binary, ternary and quaternary chalcogenides.[60] Narrow and moderate E_g of chalcogenides would help them to absorb a wide wavelength range of visible light from solar spectrum. Among the family of chalcogenides, metal sulfides

(MSs) based on Cd, Zn, In, Mo, and Ni have attracted significant attention in various photoredox reactions owing to their moderate and tunable E_g suitable for visible light absorption, and favorable band positions for most of the photocatalytic redox reactions.[61,62] However, the MSs are often hampered by photocorrosion, which is primarily induced by photogenerated holes and dissolved O_2 in the reaction medium. Photogenerated holes first ionize MS and then oxidize sulfur ions to sulfur, which eventually diminishes the activity of the photocatalyst. Dissolved O_2 present in the reaction medium may combine with photogenerated electrons to produce ROS that also accelerates the photocorrosion of MS. Various modification strategies such as coating, elemental doping, polarization engineering, defect engineering, and heterojunction construction have been employed to improve the photostability of MS.[62] Some of the interesting and representative publications that employed sulphides as photocatalyst for biomass-component-based water splitting are discussed in this section below.

The introduction of single-atom co-catalysts into photocatalysts could improve the redox abilities through charge separation, and hence increase the overall light harvesting efficiency. Selective formation of industrially important 2,5-diformylfuran (DFF) with H_2 was achieved by employing NiS_2/CdS composites as photocatalysts from an aqueous solution of HMF.[63] Theoretical and experimental studies revealed that NiS_2 as a co-catalyst plays an important role in the separation and transport of photogenerated charge carriers generated by CdS. *In situ* EPR studies revealed that a carbon-centered radical, $^{\bullet}C_6H_4O_3$, is the major reactive intermediate involved in the oxidation of HMF. The process of oxidation of HMF molecules starts with the activation of alkoxide anions evolved as a result of deprotonation of HMF by holes present on CdS followed by the formation of carbon-centered radicals along with the production of H^+ ions. Finally, these carbon radicals further reacted with the holes to produce DFF molecules. However, the co-catalyst, NiS_2 would interact with surface-adsorbed H_2O molecules to form a Ni–H bond and also serve as the active sites for H_2 production through the reduction of adsorbed H^+ ions.

The presence of a co-catalyst, Ni–NiO, has significantly enhanced the photoredox efficiency of Cd-MOF/S/Ni–NiO for water splitting and the oxidation of 2-phenoxy-1-phenylethanol.[64] Without Ni–NiO, 102 μmol g^{-1} h^{-1} of H_2 and 2.6% of 2-phenoxy-1-phenylethanone were produced along with the major products of phenol and acetophenone. However, the addition of Ni–NiO improved the H_2 production rate by an order of magnitude to 1058 μmol g^{-1} h^{-1} together with 2-phenoxy-1-phenylethanone (with a yield of 62%) as the major product, and phenol and acetophenone as minor products. Hole and $^{\bullet}OH$ free radical trapping experiments revealed that holes are the primary species responsible for the oxidation process. In the absence of Ni–NiO, the H_2 produced from water spitting undergoes hydrogenolysis with the oxidation product 2-phenoxy-1-phenylethanone to form phenol and acetophenone by breaking of the Cα–Cβ bond of 2-phenoxy-1-phenylethanone. However, in the presence of Ni–NiO, holes oxidize the benzylic C–OH bond of 2-phenoxy-1-phenylethanol, which leads to the dehydrogenation and subsequent formation of 2-phenoxy-1-phenylethanone. Ni–H species formation facilitates the desorption of nascent H_2 from the surface of photocatalysts. This process prevents the interaction of H_2 with 2-phenoxy-1-phenylethanone and its further conversion to phenol and acetophenone to break the Cα–Cβ bond of 2-phenoxy-1-phenylethanone. The presence of Ni–NiO in Cd-MOF/S/Ni–NiO has improved the light absorption and e^-–h^+ pair separation efficiency and selectivity of oxidized products.

Simultaneous production of acids, aldehydes and H_2 was obtained from HMF and furfuryl alcohol by employing a Ni co-catalyst-decorated CdS photocatalyst (Ni/CdS).[65] When the reaction was carried out in neutral water, there was a difference in the transformation rates of HMF and furfuryl alcohol to their corresponding aldehydes (DFF and furfural). DFT studies revealed that this difference was due to the stronger interaction of the –CHO group in HMF with Ni/CdS. Furthermore, when the reaction was carried out under strong alkaline conditions, a complete transformation of furfuryl alcohol and HMF to their respective carboxylates with the formation of H_2 was observed. The integration of metal nanoparticles exhibiting the LSPR effect, such as, Au, Ag, and Cu, can improve the light absorption and photoredox efficiency of pristine CdS. The hot electrons excited due to the LSPR effect of Cu nanoparticles in Cu NPs/CdS/In_2O_3 facilitated the reduction of H^+ to H_2, while In_2O_3 accelerates the oxidation of furfuryl alcohol to furfural.[66] The holes present in VB of In_2O_3 activate the α-C–H bond of furfuryl alcohol, oxidize to generate $^{\bullet}CH(OH)C_4H_3O$ radicals, and finally, activate the O–H bond, leading to the formation of furfural. Control experiments carried out by a radical trapping agents indicated that electrons and holes are responsible for the redox reaction, and there is no role for any radicals in the reaction. Surface potential changes of the photocatalyst before and after light illumination reveals that Cu NPs/CdS/In_2O_3 exhibits a better charge carrier transfer efficiency than CdS/In_2O_3 and Cu NPs/CdS. DFT calculations were employed to understand the HER and furfuryl alcohol oxidation mechanism on Cu NPs/CdS/In_2O_3. It was found that Cu sites exhibited the lowest ΔG_{*H} value (0.184 eV), indicating its exceptional *H adsorption efficiency under HER conditions. However, In_2O_3 possesses strong furfuryl alcohol adsorption tendency compared to other components (Cu nanoparticles, CdS) in the catalyst. Hence, In_2O_3 acts as both adsorption and reaction sites for the furfuryl alcohol oxidation process. Further, the DFT calculations suggested that the rate-determining step of the oxidation process is the deprotonation of the α-C–H bond followed by the formation of *R–CHO, which then undergo desorption to form furfural.

Han *et al.* fabricated S_v-chalcogenide/Ti_3C_2 photocatalysts (S_V for S-vacancy; chalcogenides = CdS, $CdIn_2S_4$, $ZnIn_2S_4$, ZnS, and $CuInS_2$) and evaluated their photoredox with photothermal capabilities in alcohol oxidation and H_2 production.[67] A representative catalyst, S_v-CdS/Ti_3C_2-2, obtained *via* the deposition of Ti_3C_2 on the S-vacancy containing S_v-CdS yields almost equal concentrations of DFF and H_2 in 5-HMF neutral water medium with a quantum yield of 47.2% at 420 nm. Strong and stable

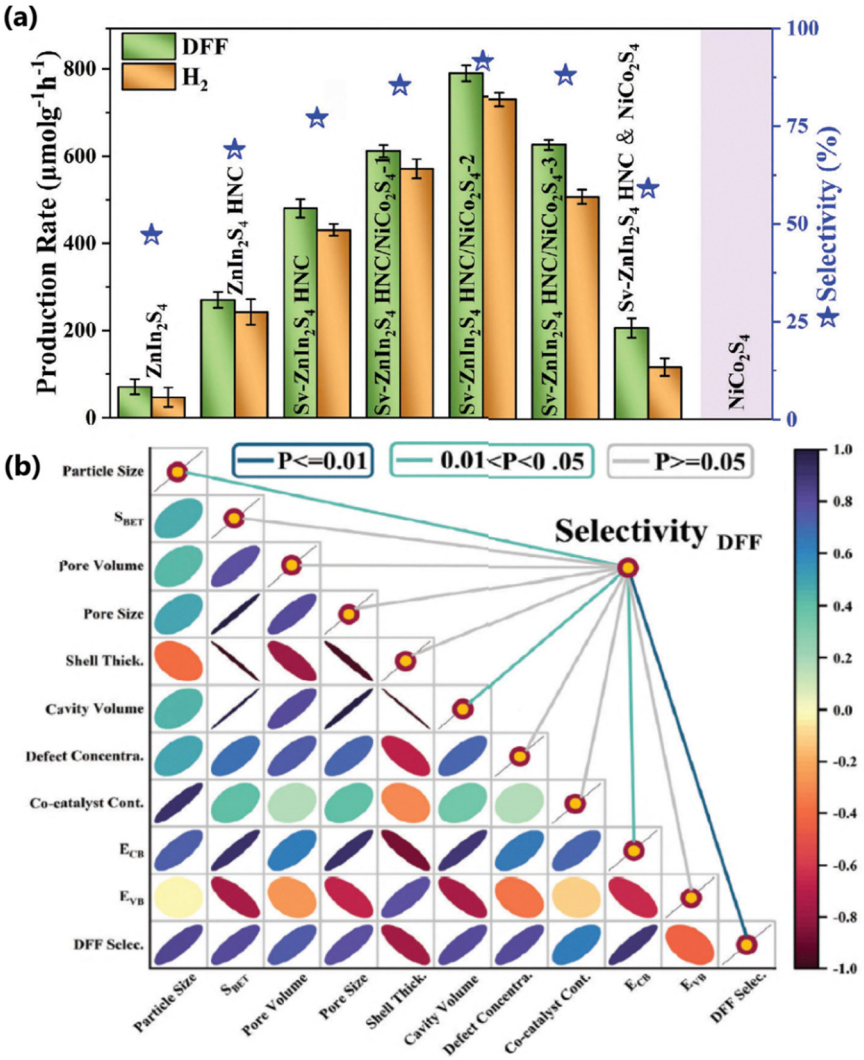

Fig. 11 (a) Photocatalytic selective alcohol oxidation coupled with H_2 evolution over the as-prepared catalysts. Parameter differences: hollow frameworks, lattice defects, interfacial chemical bonds, monocomponent/bicomponent, and component ratios. (b) Heat map of the correlation analysis between photocatalysts' physicochemical properties and DFF selectivity.[68] Reproduced with permission. Copyright 2025, Wiley.

built-in electric field (BIEF) created by the synergistic interaction between the interfacial M–O bonds and S-vacancies not only enhances the adsorption of alcohol molecules but also lowers the free energy of the intermediate state, $|\Delta G_{H^*}|$ in the H_2 production. S_v-CdS in S_v-CdS/Ti_3C_2 selectively oxidizes HMF to DFF by involving the participation of holes and •OH radicals, whereas Ti_3C_2 reduces protons from both water and alcohol to H_2. Moreover, the photoredox capability test of S_v-CdS/Ti_3C_2 for different biomass-derived alcohol entities revealed that the photocatalyst is capable of producing aldehydes/ketones from them along with H_2. The same group also developed an S_v-chalcogenide hollow nanocage/$NiCo_2S_4$ (chalcogenides include $ZnIn_2S_4$, CdS, and $CdIn_2S_4$) and evaluated the alcohol oxidation efficiency coupled with H_2 production;[68] for example, S_v-$ZnIn_2S_4$ HNC/$NiCo_2S_4$ generated 790 and 737 μmol g^{-1} h^{-1} of DFF and H_2, respectively. Defect configuration, plasma co-catalyst loading and cavity modulation have significantly enhanced the photocatalytic performance (Fig. 11a). A positive correlation was observed for the selectivity of oxidized product (DFF) and physicochemical properties such as cavity volume, microscopic pore structure, lattice defect concentration, co-catalyst loading, and band structure (Fig. 11b). $ZnIn_2S_4$ mediates the oxidation of alcohols to aldehyde and $NiCo_2S_4$ accelerates the reduction of protons to H_2. The oxidation of HMF involves both •OH radicals and holes.

A noble metal-free $Zn_{0.5}Cd_{0.5}S/MnO_2$ photocatalyst with a suitable band structure was able to produce H_2 gas with DFF *via* selective oxidation of HMF under visible and sunlight illumination.[69] The highest performing catalyst $Zn_{0.5}Cd_{0.5}S$/1%MnO_2 achieved DFF yields of 46 (in 24 h) and 14% (in 6 h) under visible and sunlight irradiation, respectively. The enhanced photocatalytic performance of the system is ascribed to the Z-scheme-aided charge transfer mechanism and synergistic interaction between $Zn_{0.5}Cd_{0.5}S$ and MnO_2. Water reduction and HMF oxidation occur at the CB of $Zn_{0.5}Cd_{0.5}S$ and the VB of MnO_2, respectively. The control experiments

using terephthalic acid (TPA) have ruled out the formation of OH free radicals, and thus, holes could be involved in the oxidation of HMF. Interstitial P-doping in $Zn_xCd_{1-x}S$ significantly enhances the generation and the life time of photogenerated charge carriers.[70] A P-doped $Zn_xCd_{1-x}S$ ($Zn_xCd_{1-x}S$-P) catalyst with rich S vacancies achieved photocatalytic H_2 production from pure water without the help of any sacrificial reagent. Moreover, the addition of HMF to this system simultaneously produced DFF and H_2. The H_2 yield increased after the introduction of DMF into the system. The enhanced activity was attributed to interstitial P-doping in $Zn_xCd_{1-x}S$ with S vacancies.

Usually, the photocatalytic oxidation of HMF yields C_6 products such as DFF by a unimolecular reaction. Kang *et al.* employed a $Ni(OH)_2$-modified $ZnIn_2S_4$ ($Ni(OH)_2$–ZIS) photocatalyst to produce C_{12} products, namely, 5,5′-dihydroxymethyl furoin (DHMF) and 5,5′-bihydroxymethyl furil (BHMF) by C–C coupling and H_2 under anaerobic condition from an aqueous solution of HMF.[71] Photoredox reaction over $Ni(OH)_2$–ZIS generates high-energy-density biofuels (DHMF and BHMF) in the diesel or jet fuel range along with H_2 by concurrent utilization of holes and electrons, respectively. A catalyst containing 2 wt% $Ni(OH)_2$ produces 2405 μmol g^{-1} of H_2 and C_{12} products with 30% yield and 79% selectivity. The photoredox efficiency of the catalyst was also tested under aerobic conditions, indicating that H_2 and C_{12} products were absent under aerobic conditions. However, DFF was produced under aerobic conditions with 43% yield and 90% selectivity, suggesting that the presence of O_2 could inhibit the formation of C_{12} products. Photogenerated electrons in $ZnIn_2S_4$ were transferred to the $Ni(OH)_2$ co-catalyst and subsequently utilized for the reduction of water. Electrons and protons in the CB of $ZnIn_2S_4$ were used for the formation of $^{\bullet}CH(OH)C_5H_5O_2$ radicals, which then undergo dimerization and converted into C_{12} products by holes present in the VB of $ZnIn_2S_4$.

A series of x% $NiS/Cd_{0.6}Zn_{0.4}S$ (x = 3, 5, 8, 10, and 15) photocatalysts selectively oxidized vanillyl alcohol to vanillin in conjunction with H_2 production.[72] The best performing catalyst, 8% $NiS/Cd_{0.6}Zn_{0.4}S$, could achieve 66.9% of vanillyl alcohol conversion to vanillin with a yield of 52.1% and a selectivity of 77.8%. The theoretical and *in situ* experimental studies revealed that the photoinduced oxidation of vanillyl proceeds through a carbon-centered radical (CH(OH)R (R = $C_7H_7O_2$)) intermediate mechanism. The activation of the α_{C-H} bond by photogenerated holes in the VB of $Cd_{0.6}Zn_{0.4}S$ was responsible for the generation of carbon-centered radicals along with the release of H^+. The carbon-centered radicals and H^+ produced from vanillyl and water are oxidized and reduced by $^{\bullet}O_2^-$ and electrons to produce vanillin and H_2, respectively. H_2 was produced at the Ni active site of NiS with a small ΔG_{H^*} value. The Schottky junction and a Ni–S–Cd electron bridge formed between $Cd_{0.6}Zn_{0.4}S$ and NiS co-catalyst with metallic properties are responsible for the enhanced photocatalytic efficiency of the hybrid material. The oxidation reactions carried out under aerobic conditions would generate reactive oxygen species, which leads to low selectivity of the desired products. However, the $Cd_{0.7}Zn_{0.3}S/NiSe_2$ composite demonstrated selective oxidation of HMF to DFF (selectivity of 98%) in conjunction with H_2 production under aerobic conditions.[73] In this composite catalyst, $Cd_{0.7}Zn_{0.3}S$ serves as a light harvesting center and $NiSe_2$ with metal-like properties acts as a co-catalyst and provides a large number of surface-active sites for H_2 production. Free radical inhibition tests and EPR technique employed in the presence of a radical scavenger (5,5-dimethyl-1-pyrroline-*N*-oxide (DMPO)) indicate that photocatalytic oxidation of HMF proceeds *via* a carbon-centered radical intermediate ($^{\bullet}CH(OH)C_5H_3O_2$). The carbon radicals thus formed are further oxidized by photogenerated holes to DFF at the VB of $Cd_{0.7}Zn_{0.3}S$.

In another work, $ZnIn_2S_4$ nanosheets anchored on CeO_2 nanosheets can simultaneously utilize both electrons and holes to generate H_2 and to oxidize furfuryl alcohol to furfural.[74] A 2D/2D S-scheme heterojunction provides broad and short channels for charge transfer. A face-to-face 2D/2D mesoporous architecture with a high specific surface area can provide a large number of reactive sites for redox reactions. Control experiments using acetonitrile (MeCN) indicated that water is the primary source of H_2, although a minor amount of H_2 was also generated during the dehydrogenation of furfuryl alcohol. The oxidation of furfuryl alcohol occurs at the VB of CeO_2 by the generation of $^{\bullet}CH(OH)C_4H_3O$ radicals and protons by holes, *via* α-C–H bond activation. These free radicals were further oxidized to furfural by powerful holes. Further, the reduction of protons from water (major) and furfuryl alcohol (minor) occurs at the CB of $ZnIn_2S_4$. The smaller Gibbs free energy of hydrogen adsorption (ΔG_{H^*}) for S sites (0.17 eV) than those for Zn and In sites implied that the S sites are the most favorable sites for the HER.

In a P–MoS_2–$ZnIn_2S_4$-2 composite (P–M–Z-2), P-doping site and sulfur vacancies act as the hole and electron trap sites, respectively.[75] This catalyst composite could effectively produce H_2 and BAD with 94% selectivity. By adjusting the concentration of P-doping, the sulfur vacancies in the composite could be controlled. The efficient redox properties of the catalyst material were attributed to the presence of the S-scheme heterojunctions with high oxidation and reduction potentials. Importantly, the optimized P–M–Z-2 displays H_2 and BAD yields of 31.4236 and 31.2977 mmol h^{-1} g^{-1}, respectively, under simulated sunlight irradiation; it underscores a near equal utilization of charge carriers for redox reactions. This work also underscores that defect engineering was one of the promising techniques to enhance the photoredox efficiency of catalysts.

A $Zn_{1-x}Cd_xS$ solid solution homojunction catalyst was used to efficiently convert sunlight into the chemical bonds through hydrogen generation (690 ± 27.6 μmol h^{-1} g^{-1}) coupled with glucose oxidation to produce lactic acid (~87% selectivity).[76] The enhanced photocatalytic performance of the catalyst was ascribed to the presence of pseudo-periodic cubic zinc blende/hexagonal wurtzite (ZB/WZ) phase in the twinning superlattice that could efficiently separate e^-–h^+ pairs. The participation of O_2^- species was ascribed to the selective production of lactic acid from glucose.

The integration of Cu–S_3 moieties (composed of single and few Cu atoms) with $Cd_xZn_{1-x}S$ is an efficient strategy to improve its photoredox capability.[77] The construction of coherent–lattice interface between Cu–S_3 and $Cd_xZn_{1-x}S$ in Cu–CdZnS facilitates the creation of a strong electronic interaction between two sulfide systems. This highly efficient photoredox system has generated 103 ± 14.6 μmol of H_2 (in 4 h) and 706 μmol of lactic acid (LA) in 25 h (with 95% selectivity) from an alkaline solution of glycerol. Cu–CdZnS also exhibited photocatalytic activity under neutral conditions, but the activity was limited compared to alkaline media. The LSPR effects induced by Cu–S_3 extended the light absorption across a broad regime (from visible to NIR). *In situ* FTIR spectroscopy revealed that the first step of oxidation of glycerol follows the conversion of glycerol to DHA followed by base-catalyzed dehydration and subsequent Cannizaro rearrangement to LA.

A ReS_2–$ZnIn_2S_4$ photocatalyst with a flower-like morphology produced furfural and H_2 from furfuryl alcohol and water.[78] Uniform loading of the co-catalyst (ReS_2) in $ZnIn_2S_4$ sheets provides a large number of active sites for photoredox reactions. The Type-I heterojunction between ReS_2 and $ZnIn_2S_4$ helps to separate electrons and holes and facilitates the flow of electrons to ReS_2 where the HER process occurs. The ratio of H_2 yield to furfural is approximately 1, suggesting nearly equal utilization of electrons and holes for photoredox reactions. The results of photocatalytic measurements using scavengers indicated that electrons and holes were the primary reactive species for the photoredox reactions.

To enhance the photoredox capability of a photocatalyst, it is advantageous to design and fabricate spatially adjacent redox-sites rather than simply focusing on the generation and separation of photogenerated charge carriers.[79] Recent studies have indicated that the spin of electrons plays a crucial role in the catalytic properties of a material. The induction of spin polarization in photocatalysts significantly improves the charge generation, separation and migration properties of a photocatalyst. Usually, photocatalysts with spin-polarized properties are obtained *via* doping with ferromagnetic ions[80] or by the introduction of cation vacancies.[81] However, the presence of excess magnetic ions could mask the active sites and the presence of a large number of vacancy sites might create recombination centers. Zhou and coworkers incorporated non-ferromagnetic Mo with non-magnetic $ZnInS_4$ to produce a ferromagnetic Mo/ZIS photocatalyst.[79] The incorporation of non-ferromagnetic Mo induces strong spin polarization within the Mo/ZIS photocatalyst system, which significantly enhances the light absorption and e^-–h^+ pair separation. The results of Bader charge analysis of Mo/ZIS indicated that Mo has a lower Bader charge value than that of In and Zn, which indicates that Mo atoms accept electrons and transfer them to S atoms under reaction conditions. This process further accelerates the accumulation of holes at the In sites, which, in turn, reduces the recombination of e^-–h^+ pairs. The calculation of adsorption energies of benzyl alcohol (ΔE_{BA}) revealed that the In site was the most favorable site for benzyl alcohol adsorption and this site holds the lowest reaction barrier for the conversion of $*C_6H_5CH_2OH$ to $*C_6H_5CHOH$ on the Mo/ZIS surface. Moreover, the presence of Mo has improved the adsorption–desorption process of H* in Mo/ZIS. Since the ΔG_{H^*} value of S_2^{2-} is lower than that of lattice S, S_2^{2-} is identified as the electron capture center as well as the reaction sites for the HER process. The spatially adjacent Mo^{5+}/S_2^{2-} and Zn sites served as optimized active sites for hydrogen production and benzyl alcohol, respectively. The presence of a special structure of Mo/ZIS photocatalyst causes the activation energy and facilitates the adsorption of reactants and the desorption of products during the reaction. The best-performing Mo/ZIS catalyst produced high H_2 and BAD yields of 172.26 and 161.46 mmol g^{-1} h^{-1}, respectively. Interestingly, under a 50 mT external magnetic field, the photocatalytic activity was further increased to 1.4 times with a selectivity of 99% towards BAD. The photoredox efficiency of the Mo/ZIS photocatalyst system for practical applications was accessed under direct sunlight, resulting in 0.98 and 0.95 mmol h^{-1} of H_2 and BAD (Fig. 12a and b). However, the H_2 produced is through the dehydrogenation of benzyl alcohol, and it is suggested to evaluate this method for water splitting too. The imbalance in the probabilities of spin up and spin down charge carriers caused by spin polarization, and spin flipping of excited electrons during transport process were responsible for the enhanced photoredox performance of Mo/ZIS in the absence of external magnetic field. In the presence of an external magnetic field, e^- and h^+ experience opposite Lorentz forces, which enhance their separation and promote the spin polarization (Fig. 12c).

The integration of atomically dispersed noble metals such as Pt with $Zn_3In_2S_6$ not only promotes the electron–hole pair separation but also helps to achieve the maximum atom efficiency.[82] The Pt_x-modified 2D–3D $Zn_3In_2S_6$ photocatalyst (x = 1–4) could selectively oxidize benzyl alcohol to BAD and reduce water to H_2. It was found that the carbon-centered radicals are formed only after the modification of $Zn_3In_2S_6$ with Pt_x. The formation of carbon-centered radicals is facilitated by holes, which is a clear indication that the presence of Pt_x nanoparticles can effectively separate photogenerated charge carriers during photocatalysis. Radical trapping and isotopic labelling experiments indicated that H atoms from water and α C–H from the PCH_2O group are dehydrogenated during the reaction. Hydrogen and BAD production occur at Pt_x and $Zn_3In_2S_6$ sites, respectively. Importantly, the photoredox system could achieve 98.2% electron-to-hole utilization efficiency. Active and sustainable hydrogen production from water during the photoredox reaction is highly advantageous to improve the kinetics of oxidation half reactions. Wang *et al.* showed that the HER rate of $ZnIn_2S_4$ could be improved by the incorporation hydrophilic phosphotungstic acid ($H_3PW_{12}O_{40}$, HPW).[83] The presence of hydrophilic HPW also enhances the fine dispersion and better wettability of the $ZnIn_2S_4$/HPW composite catalyst, which, in turn, improves the photocatalytic efficiency. The S-scheme mechanism drives the charge transfer and separation process for the HER and benzyl alcohol oxidation process. The EPR studies indicated that hydroxyl radicals ($^{\bullet}OH$) and super oxide radicals ($^{\bullet}O_2^-$) were generated, and that

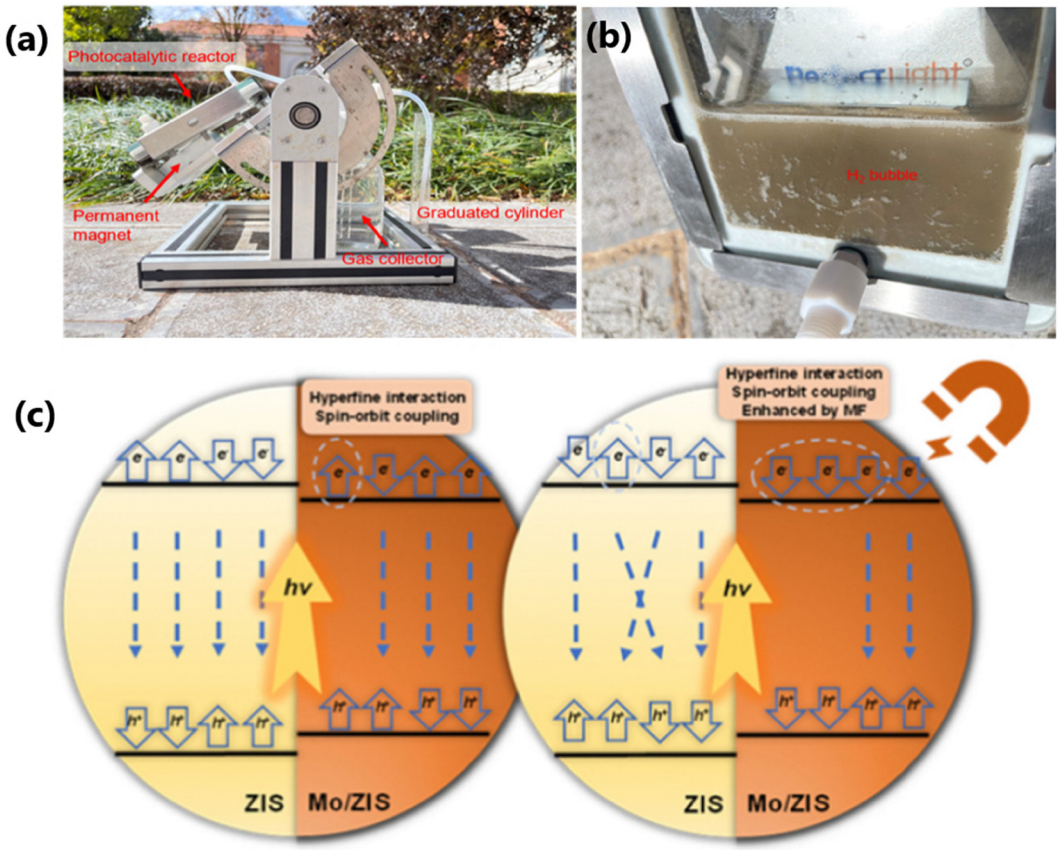

Fig. 12 (a) and (b) Outdoor photocatalytic reactor setup for H_2 and BAD production in Yunnan University. (c) Mechanism for spin polarization and magnetic field reducing photogenerated carrier recombination.[79] Reproduced with permission. Copyright 2025, Elsevier.

they participated in the oxidation of benzyl alcohol. Electron-involved water reduction and hole-involved benzyl alcohol oxidation occur at the CB of $ZnIn_2S_4$ and the HOMO level of HPW, respectively.

Low concentrations of •OH free radicals and holes with moderate oxidation efficacy are beneficial to selective conversion of benzyl alcohol to BAD.[84] The hot electrons generated by the LSPR effect created by a WC (tungsten carbide) QDs, which is decorated on defective $ZnIn_2S_4$ nanosheets, can directly participate in the water reduction to generate H_2. The differential charge density of the catalyst (DZIS/WCQDs) indicates that the electron density around WC QDs is high, which is highly beneficial for the adsorption of protons. A small amount of H_2O_2 produced during water splitting is converted to •OH free radicals by the photothermal effect of WC QDs. Photogenerated holes and •OH radicals attack the α-C–H bond of benzyl alcohol and generate the key intermediate (carbon centered radicals), which is then converted into BAD. Additionally, the photothermal effect of WC QDs generate a ''heat island'' (Fig. 13a) that could reduce the activation energy barrier for reduction process, thereby accelerating the H_2 production reaction. Detailed mechanism of photoredox reactions over WC QDs decorated $ZnIn_2S_4$ is shown in Fig. 13b. Interestingly, DZIS/WCQDs composite exhibits a high conversion rate and selectivity of 85.34 and 96.53% for BAD, and high H_2 and BAD production rates of 12.58 and 10.53 mmol g^{-1} h^{-1} without any sacrificial agent and co-catalyst.

To improve the slow charge carrier dynamics as well as bulk charge separation efficiency under photoredox conditions, Wang *et al.* developed a hollow CoS_x-modified bimetal sulphide catalyst ($Zn_xCd_{1-x}S/CoS_x$) using a sol–gel method (Fig. 14a).[85] Through this efficient method, an asymmetric structure of $Zn_xCd_{1-x}S$ is fabricated, which reflects the advantageous characteristic properties of ZnS as well as CdS. The fabrication of CoS_x with a hollow-cage-shaped architecture *via* a hydrothermal method not only provides a large surface area but also prevents the agglomeration of $Zn_xCd_{1-x}S$ nanoparticles in the composite material.

Hollow cages in CoS_x (Fig. 14b) act like an optical trap, cause multiple internal reflections within the hollow cages and eventually enhance the light harvesting efficiency of the material. The optimized catalyst, 1.6%-$CoS_x/Zn_{0.5}Cd_{0.5}S$, peaked a H_2 and a benzaldehyde yield of 20.1 and 35.2 mmol g^{-1} h^{-1}, respectively (with 100% selectivity). Isotopic labelling studies indicated that the HER process involve protons from water and benzyl alcohol. DFT calculations reveals an integration of CoS_x into $Zn_{0.5}Cd_{0.5}S$ helps to reduce the adsorption energy of benzyl alcohol, thereby reducing the energy barrier of the oxidation process, which ultimately helps to improve the overall reaction rate. The bulk phase electron–hole separation efficiency can be

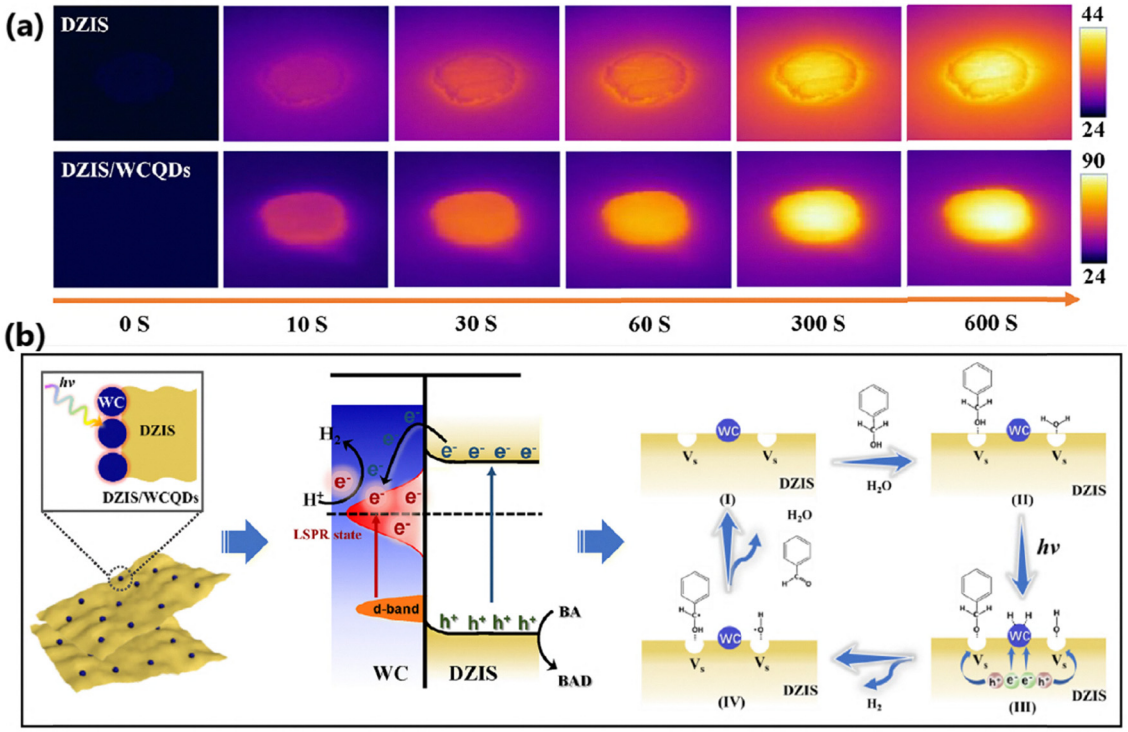

Fig. 13 (a) Infrared thermal imaging photographs of DZIS, DZIS/WCQDs and WC QDs under AM 1.5G illumination. (b) Schematic of DZIS/WCQDs for solar-driven photothermal synergistic catalytic water splitting coupled with selective BA oxidation.[84] Reproduced with permission. Copyright 2025, Wiley.

improved by creating a bulk electric field (BEF) by breaking the symmetry of atomic arrangement or creating asymmetry in the crystal structure of the photocatalyst.[86] The evaluation of potential distribution and electron transfer dynamics in $Zn_xCd_{1-x}S/CoS_x$ (Fig. 14c) indicated the coexistence of both BEF and local surface electric field (LSEF) effects, which facilitated the charge separation and charge transfer efficiency of the system during the photoredox reactions. The synergistic effect of LSEF and BEF facilitates the polarization of charge from bulk phase to surface and directs the electron flow from [Zn–S] to [Cd–S] region. The electrons in the [Cd–S] region are then migrated to the surface of CoS_x and reduce H^+ to H_2. Furthermore, holes in the VB of $Zn_xCd_{1-x}S$ break the α-C–H bond of benzyl alcohol to produce $^{\bullet}$CH(OH)Ph and H^+. The O–H bond of $^{\bullet}$CH(OH)Ph is then cleaved by another hole, leading to the formation of final products benzaldehyde and H^+. The charge transfer diagram and photoredox mechanism are shown in Fig. 14d and e, respectively.

Catalysts with a specific morphology play a significant role in their activity and selectivity.[14] One notable example is the CoP@MoS_2-*x* photocatalyst, which exhibited a flower-like morphology and demonstrated better photoredox efficiency for water reduction and xylose oxidation reactions.[87] The optimal catalyst, CoP@MoS_2-2, was able to produce 4339.39 μmol g^{-1} h^{-1} H_2 and 81% lactic acid yield, with acetic acid, formic acid, and xylonic acid as minor products. The optimum photoredox efficiency of the catalyst was observed at 40 °C and under high pH conditions. It was found that high temperatures lead to the decomposition of lactic acid and high pH leads to the formation of more number of $^{\bullet}$OH radicals. The flower-like morphology of the catalyst facilitates the diffusion of charge carriers by reducing the diffusion length and provides more active sites at the edges of the catalyst surface. Moreover, the formation of S-scheme heterojunctions aids in the electron transport and reduces the recombination of charge carriers. The work functions measured from DFT calculations for CoP and MoS_2 are 4.787 and 3.348 eV, respectively. The large difference in work function allows the transfer of electrons from MoS_2 to CoP. The $^{\bullet}$OH radicals and holes in the VB of CoP are involved in the oxidation of xylose. First, xylose undergoes isomerization to xylulose, and subsequently, glyceraldehyde and glycolaldehyde were formed by the cleavage of the C2–C3 bond. The dehydration of the glyceraldehyde molecule thus formed leads to the formation of 2-hydroxyacrolein or pyruvaldehyde (isomerized product of 2-hydroxyacrolein) followed by intramolecular Cannizzaro reaction resulting in the formation of lactic acid.

A S-scheme heterostructure composed of $NiTiO_3$ and $Cd_{0.6}Zn_{0.4}S$ prepared by a two-step synthesis procedure involving co-precipitation followed by a hydrothermal method (Fig. 15a) could drive water reduction and oxidation of furfuryl alcohol to furfural.[88] Intimate contact between $NiTiO_3$ microrods and $Cd_{0.6}Zn_{0.4}S$ interfaces (Fig. 15b) resulted in the formation of a heterostructure among them. The results of femtosecond transient absorption spectral (fs-TAS) measurements, photocurrent response and time-resolved

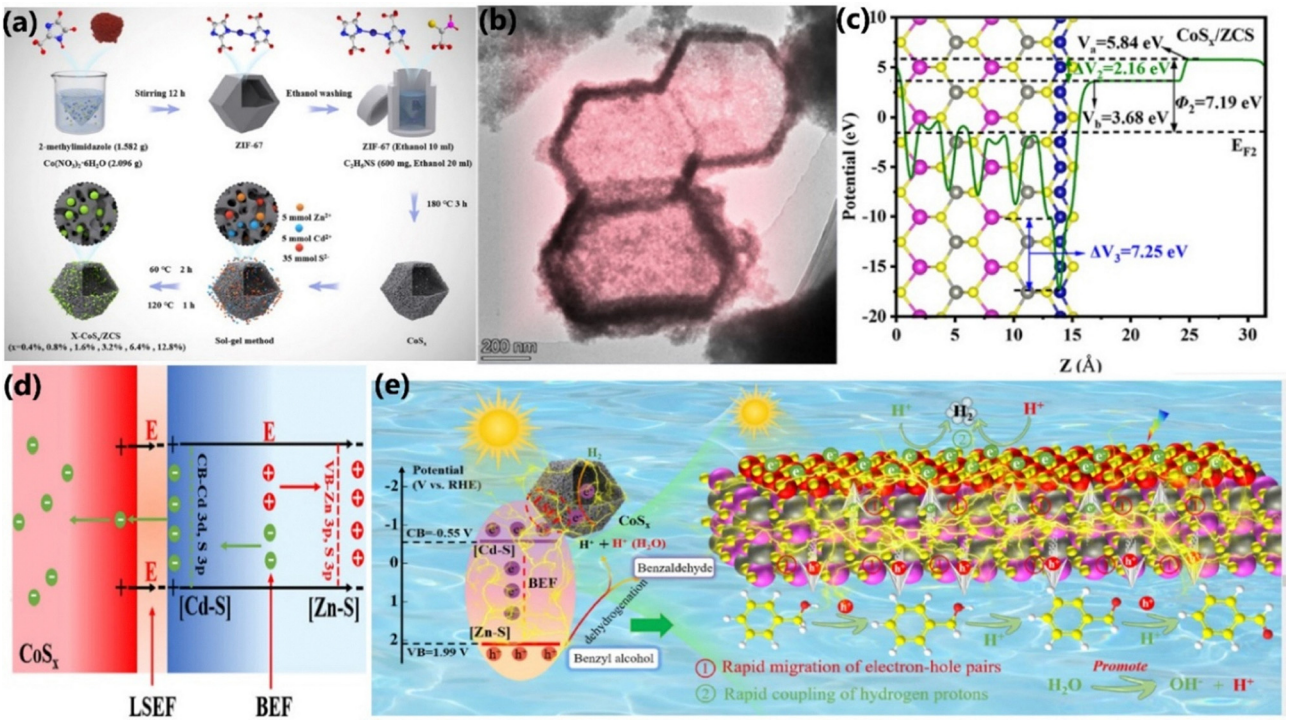

Fig. 14 (a) Preparation process diagram of ZIF-67, CoS_x and CoS_x/ZCS. (b) TEM image of 1.6%-CoS_x/ZCS. (c) Average electrostatic potential (V) distribution in CoS_x/ZCS. (d) Electron transfer mechanism diagram of CoS_x/ZCS full space electric field. (e) Mechanism diagram of CoS_x/ZCS catalyst full space electric field for efficient production of hydrogen and value-added chemicals under solar energy.[85] Reproduced with permission. Copyright 2025, ACS.

photoluminescence decay studies (Fig. 15c and d) display a long average lifetime and enhanced charge carrier transport kinetics during the photoredox reactions. The optimized $NiTiO_3/Cd_{0.6}Zn_{0.4}S$ heterostructure with a $NiTiO_3$-to-$Cd_{0.6}Zn_{0.4}S$ mass ratio of 35 has generated 4.3 and 3.3 mmol h^{-1} g^{-1} of H_2 and furfural under simulated sunlight (Fig. 15e and f). The IEF-driven charge abstraction and its oriented accumulation lead to the buildup of electrons on $Cd_{0.6}Zn_{0.4}S$ sites and the retention of holes on $NiTiO_3$ sites for water reduction and furfural oxidation, respectively (Fig. 15g–j). Moreover, *in situ* ESR and free-radical trapping experiments validated the formation of radical species $^{\bullet}O_2^-$ and $^{\bullet}OH$; however, the photogenerated holes play a key role in the oxidation of furfuryl alcohol compared to radical species. Deuterium-labeled experiments clearly verified that water is the main source of proton, and it is reduced to hydrogen at the CB of $Cd_{0.6}Zn_{0.4}S$. Meanwhile, some of the electrons and holes reacted with O_2 and water to form $^{\bullet}O_2^-$ and $^{\bullet}OH$, respectively. The holes present at the VB activate the α-C–H of furfuryl alcohol to produce carbon-centered radical intermediates, $^{\bullet}CH(OH)R$ (R = C_4H_3O), and release H^+ ions. The $^{\bullet}OH$ radicals further oxidize $^{\bullet}CH(OH)C_4H_3O$ to a geminal diol, $CH(OH)_2R$ (where R = C_4H_3O), which was further converted to furfural. The detailed mechanism of photoredox reaction is shown in Fig. 15k and l. Even though the photocatalyst system could achieve a furfuryl alcohol conversion of 72.8% in 7 h, a limited supply of air to the reaction medium could generate more number of free radical species, which ultimately leads to almost 100% conversion of furfuryl alcohol to furfural in a shorter reaction time.

6. Carbon-based photocatalysts

Carbon nitrides (CN_x), especially graphitic carbon nitride (g-C_3N_4), has gained large attention in recent years because of its unique electronic structure, suitable E_g (2.7 eV), efficiency to absorb visible light and well-aligned VB (1.4 eV) and CB (−1.3 eV) positions suitable for most of the redox reactions such as water splitting.[89] Battula *et al.* employed Pt-loaded porous carbon nitride for simultaneous hydrogen production and HMF oxidation to DFF under visible light irradiation.[90] After 6 h of reaction, 2 μmol h^{-1} m^{-2} of H_2 and 13.8% of DFF were obtained with >99% selectivity and the yield of H_2 and DFF were increased to 36 μmol h^{-1} m^{-2} and 38.4% after 48 h reaction while maintaining a selectivity of >99% for oxidized products. Experiments conducted using D_2O indicated that water is the primary source of protons and a minor amount of protons were also generated during the oxidation of HMF; ≥99% selectivity towards DFF was obtained due to the suitable VB position of the porous carbon nitride, which can oxidize OH-group of HMF only up to aldehyde (CHO) (not to COOH) in an aqueous medium. The reduction of water occurs at the Pt co-catalyst *via* the formation of Pt–H bonds and subsequent formation of H_2. Co-doping has emerged as an effective strategy to improve the conductivity and electrical properties of carbon nitride. Zheng *et al.* fabricated a K/Co co-doped carbon nitride

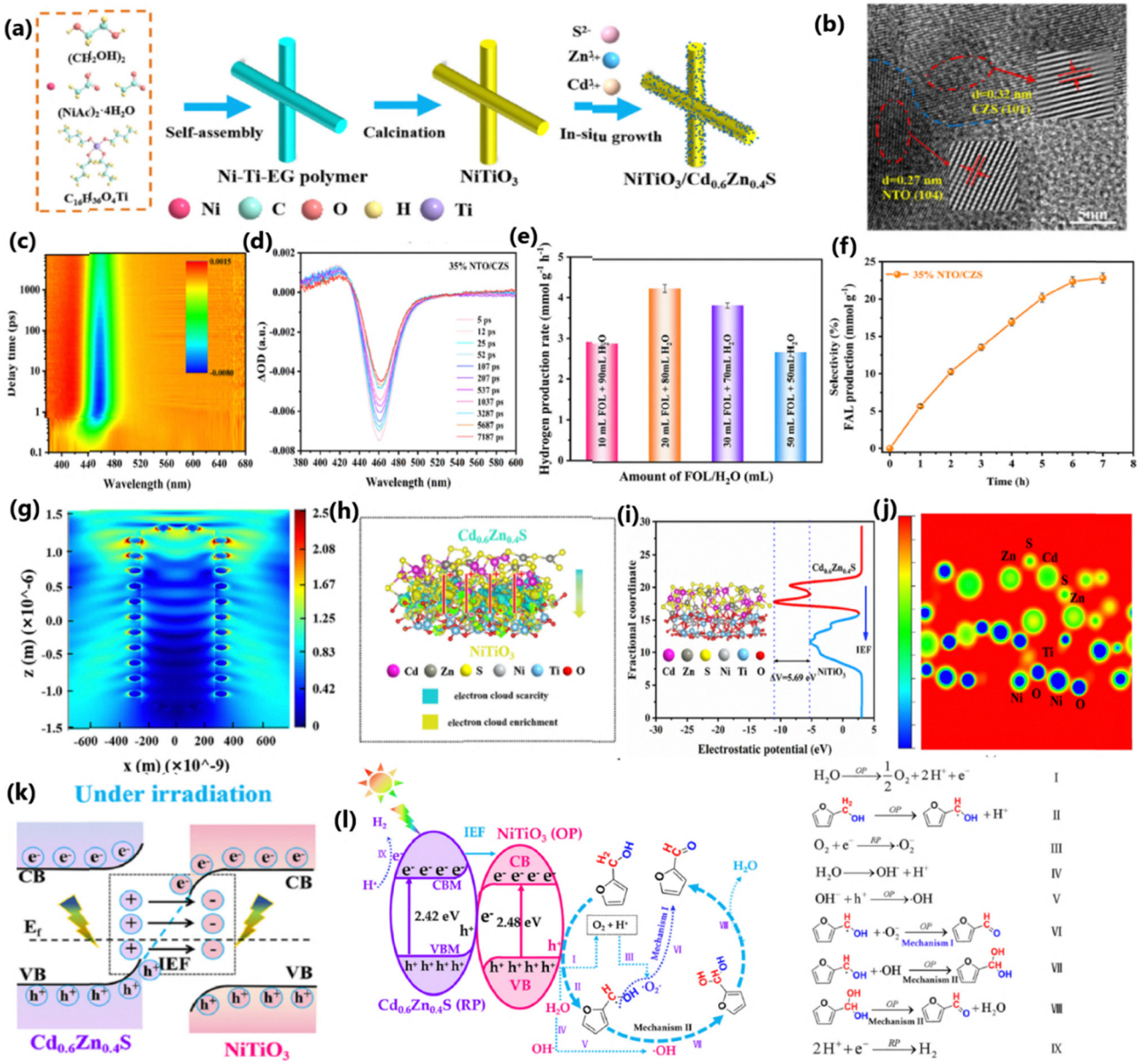

Fig. 15 (a) Schematic depicting the synthetic route of $NiTiO_3/Cd_{0.6}Zn_{0.4}S$ and (b) HRTEM image of $NiTiO_3/Cd_{0.6}Zn_{0.4}S$. (c) Two-dimensional pseudo-color of fs-TA spectra and (d) fs-TAS plots at different delay times for $NiTiO_3/Cd_{0.6}Zn_{0.4}S$. (e) HER activity of 35% $NiTiO_3/Cd_{0.6}Zn_{0.4}S$ using FAL as a hole-trapping agent in an aqueous solution with different concentrations of FAL. (f) Furfuryl alcohol oxidation performance of $NiTiO_3/Cd_{0.6}Zn_{0.4}S$. (g) Electric field distribution derived by FDTD simulation from $NiTiO_3/Cd_{0.6}Zn_{0.4}S$. (h) 3D charge density difference at the interface of $NiTiO_3/Cd_{0.6}Zn_{0.4}S$. (i) and (j) Electrostatic potential profile of $NiTiO_3/Cd_{0.6}Zn_{0.4}S$. (k) Energy band diagrams of $NiTiO_3$ and $Cd_{0.6}Zn_{0.4}S$ contacts to form 35% $NiTiO_3/Cd_{0.6}Zn_{0.4}S$ heterojunction under irradiation. (l) Photocatalytic mechanism of 35% $NiTiO_3/Cd_{0.6}Zn_{0.4}S$ heterostructure for selective oxidation of furfuryl alcohol (FOL) to furfural (FAL) coupled with hydrogen evolution.[88] Reproduced with permission. Copyright 2024, Elsevier.

(KCoCN) for tandem water splitting and furfuryl alcohol oxidation.[91] KCoCN is reported to produce 550 μmol h^{-1} g^{-1} of H_2 and 148 μmol/4 h of furoic acid with 89% conversion. The presence of K^+ ions in KCoCN facilitates interlayer spacing and enhances charge carrier separation efficiency by modulating the electronic structure, whereas Co^{2+} ions introduce redox-active sites and aid in improving both cyano functionalities and electron mobility. Electrochemical and photoluminescence studies revealed that the presence of both K and Co has significantly improved the charge transfer and photogenerated charge carrier separation efficiency. Active species trapping experiments and *in situ* FT-IR studies revealed that the electrons and holes were responsible for the water reduction and furfuryl alcohol oxidation, respectively.

Photocatalytic efficiency of carbon nitrides with poly(heptazine imide) frameworks can be enhanced by modulating the in-plane crystallinity and doping of alkali metals such as Na and K.[91,92] These modifications are highly beneficial

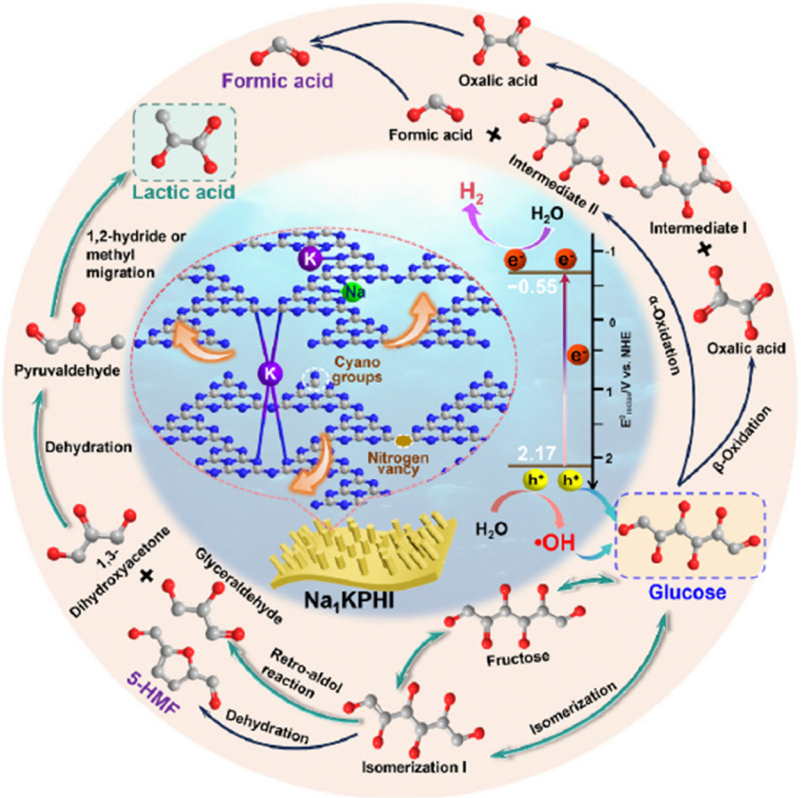

Fig. 16 Possible reaction mechanism of the photocatalytic hydrogen and glucose conversion over Na_1KPHI.[92] Reproduced with permission. Copyright 2025, Elsevier.

for charge transfer kinetics within planes and providing more active sites for redox reactions. A dual metal doping strategy creates defect sites and N-vacancies within –CN groups, which, in turn, facilitates the charge carrier migration.[92] The formation of H_2 and lactic acid (71.2%) *via* water splitting and glucose conversion involves charge carriers and •OH radicals with 98.7% overall conversion. H_2 production and lactic acid generation in 1 M KOH is a further indication of the photoredox capability of the catalyst system under alkaline conditions (see Fig. 16). The C/N ratio in melon-based carbon nitrides (CNs) has great significance in the light absorption and harvesting abilities of CNs.[93] The optimum C/N ratio is required to attain simultaneous H_2 production and selective oxidation of HMF to DFF with more than 90% selectivity. DFT, PL and TRPL studies revealed that the adsorption of HMF molecules has modified the charge separation efficiency, and thus, the photoredox efficiency of the photocatalyst.

An *in situ* generated p–n junction was created by the deposition of in situ-generated Mn_3O_4 on crystalline carbon nitride sodium poly(heptazine imides) (Na-PHI). Further deposition of Pt enhances the photoredox efficiency of the catalyst system.[94] Electrons trapped by Na-PHI complete the H_2 production with a Pt co-catalyst, whereas holes in Mn_3O_4 trigger the oxidation of benzylamine. *In situ* EPR studies using trapping agents revealed that $C_6H_5CH_2NH_2^{\bullet+}$ radicals formed during the coupling oxidation of benzylamine by holes were the main active species for the formation of N-benzylbenzaldimine (with 70% selectivity). Mass transportation at the solid–liquid interface involving polymeric carbon nitride can be solved by incorporating electron-deficient pyromellitic dianhydrides (PMDA).[95] PMDA in CN_x induces the formation of mesoporous channels and facilitates the mass transport of benzyl alcohol. Experiments conducted in the presence of radical scavengers indicated that photoredox reactions proceed *via* two paths such as direct and radical mediated oxidation. Under direct oxidation, holes oxidize benzyl alcohol to BAD, while in the second pathway, holes oxidize water and benzyl alcohol to •OH and carbon-centered radicals. These radicals interact with each other to produce BAD, meanwhile the protons released from benzyl alcohol and water were reduced to H_2. The IEF constructed in CN by PMDA drive the efficient separation and transport of charge carriers and subsequently helps to attain a STH conversion efficiency of 2.15%.

6.1. g-C_3N_4-based photocatalysts

Doping of non-metals such as C, O, S, and P into g-C_3N_4 considerably improves the light-harvesting efficiency of g-C_3N_4.[96] Especially, doping with P has received considerable attention due to the formation of P–N linkages and N–P–N–C channels, which act as an efficient migration channel for photogenerated charge carriers. Moreover, the presence of delocalized orbitals around P and N-atoms aids the separation of e^-–h^+ pairs during the reaction. P-doped g-C_3N_4 was prepared through the thermal condensation of dicyandiamide

(DCDA) and an inositol hexaphosphate (IP6) as the P-source.[97] The results of control experiments show that the selective formation of BAD from benzyl alcohol proceeded through a carbon-centered radical route. The optimized catalyst (CN-210P) produced 51.6 and 64.2 μmol $h^{-1}g^{-1}$ of H_2 and benzaldehyde, respectively. DFT studies show that P-dopants preferentially substitute the C-site rather than the N site of the tri-*s*-triazine ring of g-C_3N_4. This process eventually leads to the formation of mid-gap states located near the E_F, which enhance the visible-light absorption and photoredox efficiency of P-doped g-C_3N_4.

A Ni–Au bimetal-modified g-C_3N_4 (Ni–Au/g-C_3N_4) photocatalyst was used for the co-production of H_2 and furfural from aqueous furfuryl alcohol.[98] In this photocatalyst system, the combined effect of g-C_3N_4 nanosheets and plasmonic Au was responsible for the enhanced light-harvesting and utilization efficiency of the material. The Schottky junction formed at the interface between Au and g-C_3N_4 helps to separate photogenerated electron–hole pairs. The Ni species serve as both the electron capture center and the active sites for the reduction of H^+ generated from furfuryl alcohol and water. Further, the holes residing on g-C_3N_4 could generate $^{\bullet}$OH radicals and carbon-centered radicals from hydroxyl and furfural alcohol molecules, respectively. The radical species formed in the previous step ($^{\bullet}$OH radical and carbon-centered radical) react together to form furfural along with the release of H_2O molecules. Therefore, the recycling of H_2O molecules within the reaction medium would mutually promote the photoredox reactions. $LaVO_4$/g-C_3N_4 ($LaVO_4$/CN) heterostructure could produce 0.287 mmol g^{-1} h^{-1} of H_2 and 0.95 mmol g^{-1} h^{-1} of furfural from furfuryl alcohol. The 2D/2D heterointerfaces created by square-shaped $LaVO_4$ nanoflakes and g-C_3N_4 nanosheets effectively separate electron–hole pairs.[99]

A Pt-loaded polymeric C_3N_4 photocatalyst (Pt–C_3N_4) was employed for the photoreforming of glucose into hydrogen and lactic acid with 100% conversion efficiency and 86% selectivity.[100] The pH dependence of glucose photoreforming indicates that this process is more favorable at higher pH. Highly alkaline conditions facilitate the generation of a large number of hydroxyl ions, which leads to the potential oxidation of glucose molecules. The HER performance of the catalyst system depends on the concentration of Pt. Specifically, the HER decreases at higher Pt loadings. The photoreforming efficiency of the Pt–C_3N_4 catalyst was tested with different lignocellulose derivatives such as cellulose (fructose and α-cellulose), hemicellulose (furfural, xylose and xylan), lignin (guaiacol and alkali lignin). The observed HER follows the decreasing order: cellulose > hemicellulose > lignin. Interestingly, the photoreforming of furfural could produce xylose and xylan together with H_2. The DFT studies revealed that the presence of Pt on the surface of C_3N_4 decreases the activation energy barriers for water splitting reaction and facilitate the generation of H_2 from adsorbed protons. The most active Pt-sites for the HER in the Pt-loaded polymeric C_3N_4 photocatalyst (Pt–C_3N_4) was analyzed by calculating the Gibbs free energy of adsorption (ΔG_H) values of Pt-atoms from different layers. Surface Pt atoms show the lowest ΔG_H value compared to second- and third-layer Pt-atoms, indicating that upper layer Pt-atoms are more efficient sites for the HER process; this was experimentally and separately confirmed by Bajpai *et al.*[101] by coating 0.5 monolayer of Pt on a NiCu alloy. Moreover, the calculation of Gibbs activation energy barriers indicates that the incorporation of Pt-atoms significantly lowers the activation energy of water splitting and hence boosted the HER performance of the catalyst system. The selective production of lactic acid was obtained by the cleavage of the C–C bond of the fructose molecule, which was formed during the glucose isomerization step.

Polymeric carbon nitride (PCN) materials gained large attention in the field of photocatalysis due to their favorable band positions and visible light absorption efficiencies.[102] Nevertheless, the increased recombination rate of charge carriers, arising from the delocalization of electrons due to their highly symmetrical molecular structure, has a limited photooxidation efficiency of PCN. The integration of P–N_3 group with PCN has increased the number of catalytically active sites, induced charge asymmetry, and promoted the polarization of local charge.[103] Moreover, the asymmetric charge distribution facilitates the separation of charge carriers. The optimized P–N_3-modified narrow-dimensional fragmented carbon nitride (P-CNNS) photocatalyst produces 27.9 mmol g^{-1} of H_2 (with 1 wt% Pt co-catalyst) and 13.5 mmol g^{-1} of anisaldehyde (AA) in 12 h from aqueous 4-methoxybenzyl alcohol (4-MBA). Liquid chromatography analysis revealed that about 85% of 4-MBA is selectively converted to AA within 12 h. Charge polarized sites in P-CNNS, introduced by P–N_3, activate 4-MBA and facilitate the adsorption of reactant molecules and selective conversion to AA. Enhanced dual functionality of the photocatalyst system is due to the presence of a large number of surface-active sites and reduced charge carrier migration distance arising from large specific surface area, narrow morphology, and a large number of pores within P-CNNS.

The production of H_2 and lactic acid as well as the stability of lactic acid in the photoredox reaction of the water-xylose reaction medium was found to be enhanced by carrying out this reaction in an alkaline medium containing the optimum NaOH concentration of 2 mol L^{-1}.[104] At a higher NaOH concentration, the conversion of xylose reaches up to 95.4%; however, the yields of lactic acid and H_2 tend to decrease. The non-availability of H^+ ions decreases the HER rate, thereby reducing electron utilization for reduction. Consequently, the e^-–h^+ recombination rate increases, leading to the decline in the oxidation rate of xylose. The presence of Pt–N coordination bonds in a single Pt-atom-anchored imidazole ring-incorporated g-C_3N_4 photocatalyst helps to produce an H_2 and a lactic acid yield of 271.9 μmol/4 h and 499 μmol/4 h (corresponding to a yield of 89.9%), respectively, under simulated sunlight. Anchoring both imidazole rings and isolated Pt atoms within the g-C_3N_4 framework enhances the electron density around E_F and improves the light absorption and harvesting efficiencies. This again provides a large number of efficient and exposed photoredox sites for coupled reactions.

Selective and efficient oxidation of xylose to lactic acid involves $^{\bullet}O_2$, $^1O_2$ and holes, and this reaction proceeds *via* the formation of a $^{\bullet}C_5H_9O_5$ radical intermediate by the C–C bond cleavage of xylose. The $^{\bullet}C_5H_9O_5$ radicals thus produced undergo C_3–C_4 cleavage by $^{\bullet}O_2$, $^1O_2$ and holes to produce glycolaldehyde and glyceraldehyde. Glyceraldehyde was then subjected to isomerization to form DHA, and subsequently, the DHA and another molecule of glyceraldehyde undergo dehydration to form pyruvaldehyde. Finally, the rehydration of pyruvaldehyde produces lactic acid. As the CB position of the photocatalyst (−1.04 V *vs.* NHE) is more negative than H^+/H_2, it easily facilitates water reduction to H_2. The presence of NaOH helps to stabilize the final product due to the formation of sodium lactate.

Sun *et al.* developed a phosphorus/oxygen co-doped carbon nitride photocatalyst for water splitting with aqueous monosaccharide that exhibits concurrent H_2 and lactic acid production.[105] The photocatalytic studies in the presence of different monosaccharides (xylose, glucose, fructose, mannose rhamnose and arabinose) revealed that mannose and xylose were the optimal substrates for H_2 generation and lactic acid production, respectively. The studies under different alkaline concentrations indicated that low alkalinity promotes H_2 production, while high alkalinity favors lactic acid production. Control experiments revealed that $^{\bullet}O_2^-$, $^{\bullet}OH$, $^1O_2$ and holes were beneficial for the production of lactic acid, and $^{\bullet}O_2^-$ played a major a role in this process. The same research group has evaluated the effect of co-doped Zn/O-atoms with incompletely polymerized graphitic carbon nitride towards synchronous photoredox reactions involving water splitting and lactic acid production by reforming monosaccharides under white LED light irradiation.[106] Like the previous study, they evaluated the photocatalytic efficiency of the catalyst system in an aqueous solution of different monosaccharides and found that comparatively higher H_2 production and lactic acid yield were obtained with arabinose and glucose. These results are different from the previous study, and it was concluded that different co-dopants show distinct photocatalytic efficiency with the same biomass derivatives. The results of control experiments and ESR spectroscopy measurements (Fig. 17a–f) revealed that $^1O_2$, $^{\bullet}O_2^-$, $^{\bullet}OH$, and h^+ are involved in the production of lactic acid. The reaction pathway for H_2 production and xylose conversion in the xylose-alkali solution over Zn_2/O@IP-g-CN is shown in Fig. 17g.

Initially xylose molecules undergo isomerization reaction to produce intermediate I, which was further converted to oxalic acid and intermediate II. Oxalic acid formed in the earlier step was then transformed to glyceraldehyde and finally to lactic acid. However, oxalic acid was converted into formic acid *via* the C–C bond cleavage. Intermediate I or II is converted to intermediate III and acetic acid *via* α-oxidation, and in a similar way, intermediate I or II is converted to formic acid by a β-oxidation reaction.

The integration of single-atom Pd in g-C_3N_4 (Pd_1/BCN_x) leads to the formation of a Pd–N coordinate bond between Pd atoms and g-C_3N_4.[89] The presence of interlayer Pd–N_4 coordination stabilizes the isolated Pd single atoms and boosts the charge carrier separation and transfer kinetics for coupled redox reactions. This was supported by DFT calculations, *i.e.*, the electrons were distributed on the in-plane heptazine unit-free C_{ring} and Pd atoms in the LUMO, whereas holes were distributed on the in-plane heptazine units involving C_{ring} in the HOMO. Photoredox reactions involving H_2 production, and xylose and fructose conversion in alkaline and alkaline-free media indicated that both the H_2 production, and xylose and fructose conversion efficiencies were increased in the former case. Both monosaccharides produce lactic acid as the main product along with H_2. In the presence of xylose and fructose, xylonic acid and gluconic acid were obtained as the by-products, respectively, along with the intermediates such as glyceraldehyde, glycolaldehyde, DHA, and pyruvaldehyde. Even though light irradiation over 6 h resulted in an increase in the H_2 yield, it led to over-oxidation of fructose and xylose to by-products, gluconic acid and xylonic acid, respectively, and ultimately with extensive C–C cleavage to formic acid and then to CO_2. Hence, long-term light irradiation gradually leads to a decrease in the concentration of major product (lactic acid), due to its secondary reactions over extended periods.

6.2. Graphene oxide-based photocatalysts

The photocatalytic reforming of cellulose into H_2 and $HCOO^-$ was accomplished using a Pt cocatalyst integrated into S- and N doped graphene oxide dots (SNGODs) with GO sheets.[107] This work elucidated the detailed mechanism of redox reaction associated with the photoreforming of cellulose. Under a strong alkaline medium (10 M NaOH), water-insoluble cellulose was decomposed by piece-by-piece peeling of its constituent D-glucose units. These peeled-off units were then converted into deprotonated C6 molecules (isosaccharinic acid), which then transformed into C_5–C_1 molecules with $HCOO^-$ as the major end product. Isotopic studies revealed that H_2 was generated from water rather than cellulose during the oxidation of C_6 derivatives. A stable photocatalytic H_2 production over a period of 6 days with 35% of cellulose reforming was accomplished. The stable HER was attributed to the high nitrogen content that eliminated the vacancy defect sites on basal plane; this ensures the stable transport of electrons to GO sheets for the HER. The intimate contact between the GO dots and cellulose molecules facilitates the rapid injection of holes to the cellulose derivatives for their oxidation; this process leads to the suppression of the formation of $^{\bullet}OH$ radicals. The selectivity of products obtained after the photoreforming of biomass components highly depends on the nature of co-catalysts.

The integration of Pt and Ag co-catalysts with SNGODs for the photoredox reactions involves the reduction of water and photoreforming of xylose, which indicated that Pt was more effective in HER compared to Ag.[108] Pt-loaded SNGODs exhibited 7.7 times higher HER activity compared to Ag-loaded SNGODs (Fig. 18a). Photoreforming of xylose Pt-SNGODs could produce C_1–C_5 products and a moderate amount of C_6 products. However, Ag-SNGODs convert xylose into C_1–C_3 and C_6 products. With a Pt-cocatalyst, the photocatalyst system generated 14 varieties of products (formate is the major product),

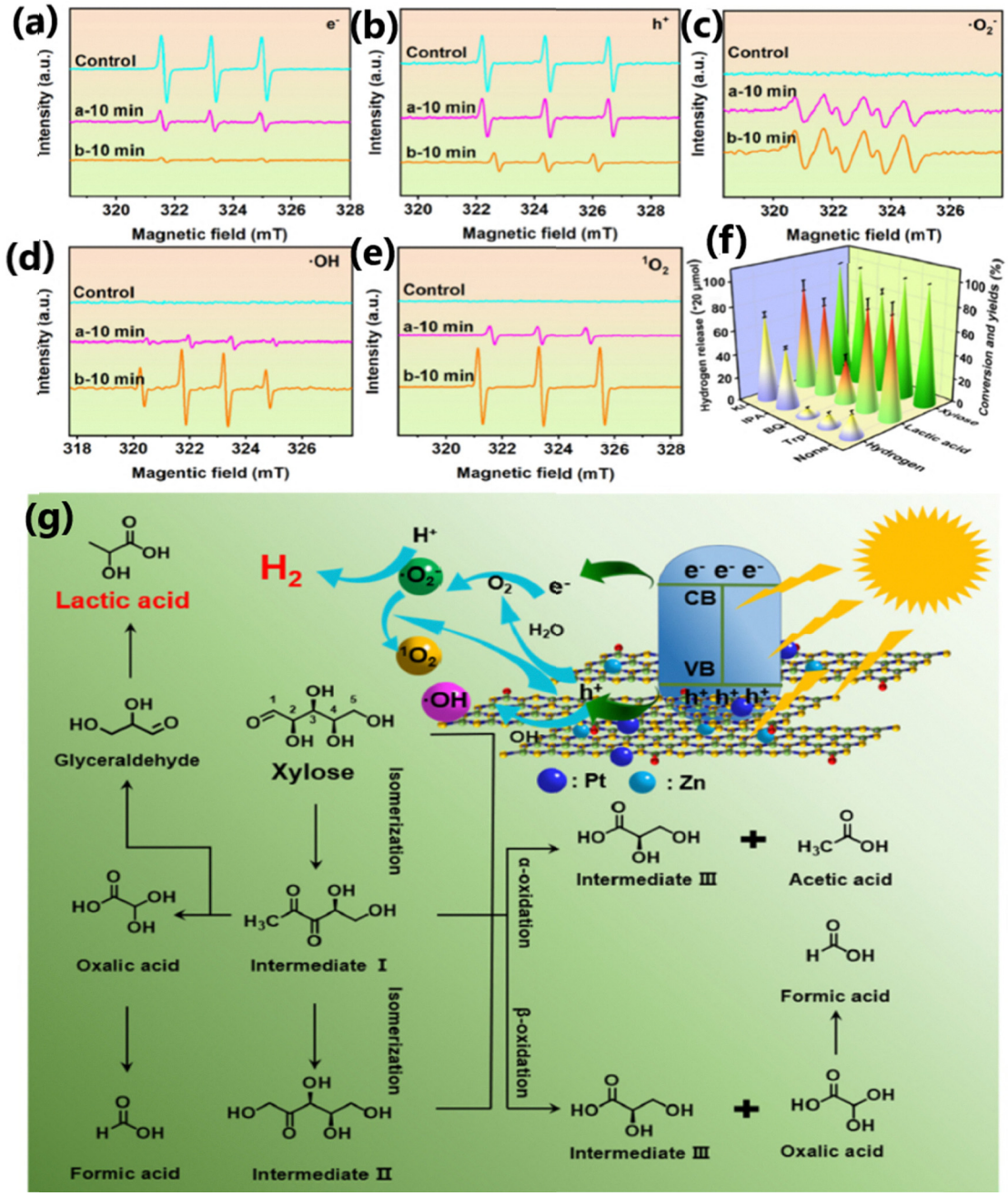

Fig. 17 TEMPO ESR spin-labeling experiments for (a) electrons and (b) holes. DMPO ESR spin-trapping experiments for (c) $^{\bullet}O_2^-$, (d) $^{\bullet}OH$ radicals, and (e) TEMPONE ESR spin-labeling for $^1O_2$ for CN and Zn_2/O@IP-g-CN. (f) Effects of different active radicals on the hydrogen release and lactic acid production using the Zn_2/O@IP-g-CN photocatalyst. (g) Possible reaction pathway of the co-production of hydrogen and lactic acid over the Zn_2/O@IP-g-CN photocatalyst.[106] Reproduced with permission. Copyright 2022, Elsevier.

while with Ag-cocatalyst, 9 varieties of liquid products were obtained (gluconate is the major product) after 72 h of reaction (Fig. 18b). Photoredox reaction mechanism with Pt-cocatalysts proceeds *via* the reduction of water on the surface of Pt to produce H_2. Due to the attraction between electron-rich oxygen of the formyl group and h^+-loaded SNGOD, the oxidation of xylose occurs on its aldehyde end. Furthermore, the HER cannot proceed with Ag-SNGODs, due to the accumulation of electrons on the catalyst surface rather than electron donation for H_2 formation. The accumulated electrons interact with the OH-group of the third carbon of xylose and lead to the formation of reaction intermediates, glycolaldehyde and glyceraldehyde, *via* a retro-aldol reaction mechanism. These two reaction intermediates were then decomposed to C_3–C_1 and the linear-form xylose (r-C_5) reacts with C_1 to form a C_6 product (gluconate). Ag-SNGOD is less active for the HER, and

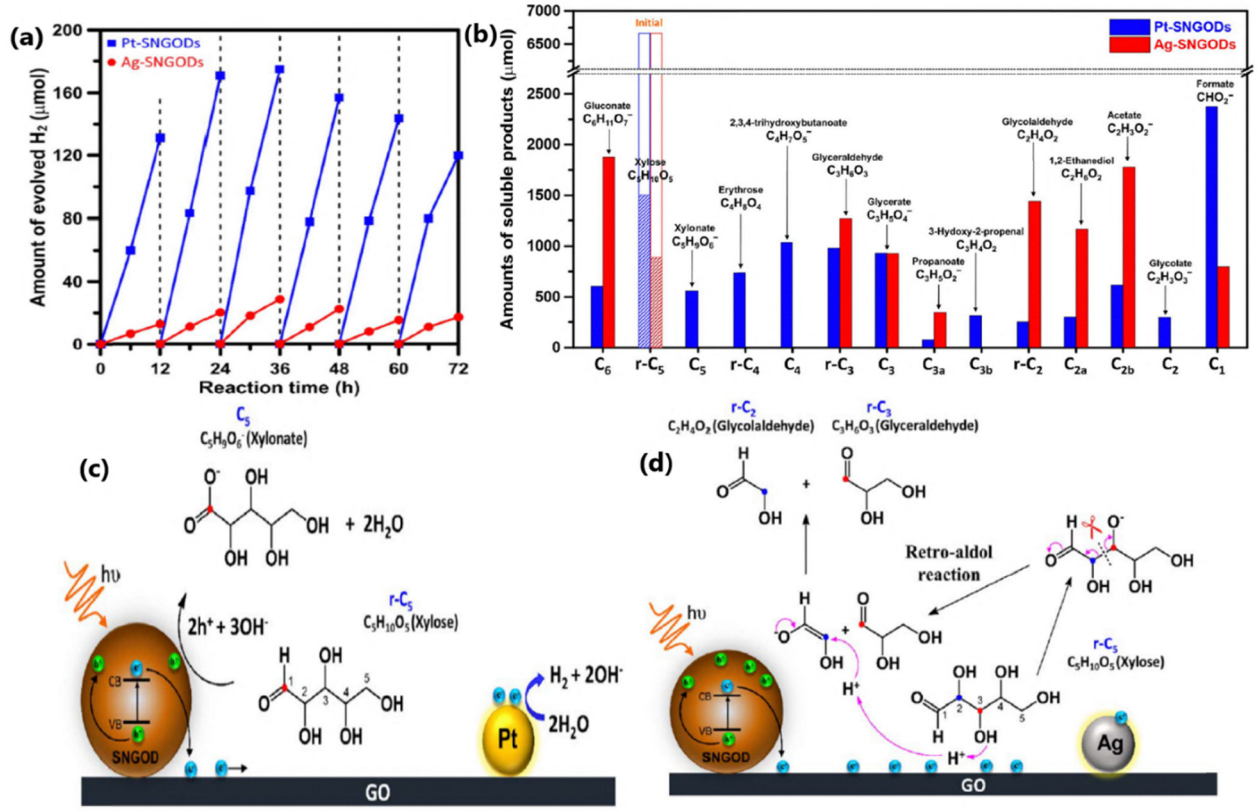

Fig. 18 (a) Evolution of H_2 from xylose solutions containing Pt-SNGODs and Ag-SNGODs under simulated solar irradiation (AM 1.5, 100 mW cm^{-2}). (b) Product compositions in the liquid phase after the photocatalytic reforming of xylose for 72 h. The charge distributions of the SNGODs is shown when associated with different co-catalysts; (c) Pt co-catalyst for oxidative xylose reforming (Pt-SNGODs were active in consuming photogenerated electrons for H_2 evolution), and (d) Ag co-catalyst for retro-aldol reaction (Ag-SNGODs were less effective in HER).[108] Reproduced with permission. Copyright 2024, RSC.

photogenerated electrons participate in the cleavage of xylose to produce C3- and C2-species, and they were further reformed into C3–C1 species. The charge distributions of the SNGODs loaded with Pt and Ag during the photoredox reactions (HER coupled with oxidation of xylose) are shown in Fig. 18c and d.

A brief summary of photoredox efficiency of various photocatalyst systems reported, reaction conditions, products obtained, *etc.*, discussed throughout the review manuscript is concisely provided in Table 1 for H_2 evolution coupled with oxidation of biomass components to VAPs.pt

7. Conclusions and future perspectives

In this review article, the recent progress of water splitting photocatalysis coupled with the oxidation of biomass components to produce green H_2 and VAPs concurrently is discussed and summarized. This rapidly developing, interesting and necessary field of photocatalysis replaces the sluggish OER process, which, in turn, enhances the rate of overall photoredox reactions, and taking the field to the next higher level. The present strategy has several advantages over the conventional overall water splitting process. It efficiently (a) utilizes photogenerated electrons and holes to produce green H_2 and VAPs, respectively; (b) ensures the maximum and concurrent utilization of the charge carriers; (c) the above-mentioned point enhances the long-term operation or sustainability of the photocatalyst materials, improving the economic aspects of overall photocatalytic redox process; (d) in view of the low (and small amount) and high molecular weight (and large amount) of H_2 and VAPs, respectively, the former appears to be a minor product (in terms of value and quantity), compared to the VAPs. When there is further positive growth in this field towards technology development/demonstration, some of the chemicals currently produced by conventional chemical/catalysis methods (formate and glyceric acid) are likely to shift to the photocatalysis process discussed throughout the review. Hydrogen production and biomass valorization *via* conventional heterogeneous catalysis methods are invariably associated with environmental issues. The utilization of abundant natural resources like water and sunlight for biomass conversion together with H_2 production has the potential to achieve carbon neutrality and environmental sustainability.

Three sets of materials were widely employed in the photocatalysis of biomass component-based photocatalysis reactions. Metal oxides, like TiO_2, with appropriate CB and VB positions are suitable for the co-production of H_2 and VAPs. However, the integration of TiO_2 (or any wide E_g semiconductor) with a suitable visible light-absorbing semiconductor along

Table 1 Comparison of the photoredox efficiencies of various photocatalyst systems for concurrent H_2 evolution and oxidation of biomass components to VAPs

Photocatalyst	Reaction conditions and light source	H_2 yield (mmol g^{-1} h^{-1})	Value added products (Yield)	Selectivity of major liquid product (%)	AQE (%)	Stability/ cycling stability	Ref.
TiO_2–CoNiP	Aqueous glycerol solution (5 v/v%); one sun condition (450 W solar simulator (100 mW cm^{-2}) coupled with an AM 1.5 filter)	2.027	Glyceric acid (67 mmol/25 h g), DHA, glycolaldehyde, lactic acid, and formic acid	Glyceric acid (85)	6.81	25 h	5
1% Cu/TiO_2	5% (0.6 M) glycerol in water; one sun condition (100 mW cm^{-2} with an AM 1.5 filter)	13.8	Glycolaldehyde (47.6 mmol/25 h g), formic acid (11.14 mmol/25 h g), DHA (4.5 mmol/25 h g), and glyceraldehyde	Glycolaldehyde (70)	NA	25 h	10
Au@TiO_2	5 mL (0.0.05 M) glycerol in water; under direct sunlight (60 mW cm^{-2})	32	DHA (0.6 mmol g^{-1} 5 h); glycolaldehyde (1.6 mmol g^{-1} 5 h); formic acid (0.85 mmol g^{-1} 5 h)	Glycolaldehyde (52)	NA	5 h	40
NiO/TiO_2	10% (v/v) glycerol-water solution; 300 W Xe lamp	8	Glyceraldehyde and DHA	NA	NA	24 h	49
NiO/Ti^{3+}–TiO_2	5% (v/v) aqueous glycerol solution; direct sunlight	15.62	DHA (0.80 mmol h^{-1} g^{-1}); glycolaldehyde (1.17 mmol h^{-1} g^{-1}); formic acid (0.32 mmol h^{-1} g^{-1})	Glycolaldehyde (51.1)	4.28	5	30
$BiVO_4$-QDs-TiO_2 thin film	20 mL aqueous glycerol solution (100 mM glycerol) condition; one sun condition (100 mW cm^{-2} with AM 1.5 filter)	2.87 μmol h^{-1} g^{-1}	Glyceric acid (580 mmol h^{-1} g^{-1})	Glyceric acid (98)	0.25	25 h	56
$BiVO_4$-QDs-TiO_2 thin film	20 mL aqueous glycerol solution (1 mM glycerol) in anaerobic condition; one sun condition	N/A	Lactic acid (180 μmol/3 h cm^2)	Lactic acid (100%)	0.25	3–25 h	56
NiS_2/CdS	Aqu. sol. 5-HMF (5 mM); 300 W Xe lamp with ≥420 nm filter	0.476	2,5-Diformylfuran (DFF) (519 μmol g^{-1} h^{-1})	DFF (95.2)	NA	30 h	63
S_v-CdS/Ti_3C_2	10 mL of 10 mM 5-HMF aqueous solution; 300 W Xe lamp ($\lambda \geq$ 420 nm)	0.6542	DFF (677.5 μmol g^{-1} h^{-1})	DFF (93.6)	47.2	12 h	67
S_v-$ZnIn_2S_4$HNC/$NiCo_2S_4$	10 mL 5-HMF (10 mM); Xe lamp with a UV-cut filter	0.737	DFF (790 μmol g^{-1} h^{-1})	DFF (90.8)	NA	7	68
$Zn_{0.5}Cd_{0.5}S$/1%MnO_2	2 mg mL^{-1} of 5-HMF in 20 mL water; 30 W white LED bulb (≥400 nm)	1.32 mmol/ 24 h g	DFF (46%)	DFF (100)	24.5	5	69
$Ni(OH)_2$–ZIS	10 mL of 10 mM of 5-HMF; 300 W Xe lamp (λ > 420 nm)	2.405 mmol g^{-1}	DFF (43%)	DFF (90)	0.14	5	71
Porous carbon nitride (SGCN)	0.1 mmol of HMF in 10 mL water; one sun condition 100 mW cm^{-2} (AM 1.5)	36 μmol h^{-1} m^{-2}	DFF (38.4%)	DFF (>99)	NA	48 h	90
$ZnIn_2S_4$/$W_{18}O_{49}$	60 mL of 1 vol% benzyl alcohol solution; 300 W Xe lamp	122 μmol h^{-1}	Benzaldehyde (106 μmol h^{-1})	Benzaldehyde (100)	7.64	16 h	57
Mo/$ZnIn_2S_4$ (Mo/ZIS)	1 mL of benzyl alcohol in 100 mL water; 300 W Xe lamp	172.26	Benzaldehyde (161.46 mmol g^{-1} h^{-1})	Benzaldehyde (99)	42.4	4	79
2.14% Pt/$Zn_3In_2S_6$	0.2 M benzyl alcohol; 300 W Xe lamp with 420 nm cutoff filter	0.1581 mmol h^{-1}	Benzaldehyde (165.9 μmol h^{-1})	Benzaldehyde (>93)	4.6	12 h	82
ZnS/TiO_2	5 mmol of benzyl alcohol in 50 mL water; 300 W Xe lamp for 5 h	15.23	Benzaldehyde (NA)	Benzaldehyde (88.5)	25.2	4	54
C_3N_4-/pyro mellitic dianhydride	40 mL of aqu. sol. containing 15 mL of benzyl alcohol; 300 W Xe lamp (400 nm $\leq \lambda \leq$ 780 nm)	13.87	Benzaldehyde (7.71 mmol h^{-1} g^{-1})	NA	48.21	5	95
8% NiS/$Cd_{0.6}Zn_{0.4}S$	100 mL of aqueous solution of vanillyl alcohol; 300 W Xe lamp	3.84	Vanillin (3.75 mmol g^{-1} h^{-1})	Vanillin (77.8)	2.99	9 h	72
$0.5\theta_{Pt}$ − PdTO/TiO_2	Aqu. solution of 2-butanol (10 mM); one sun condition (100 mW cm^{-2} with AM 1.5 filter)	16.2 μmol/4 h mg	2-Butanone (13.6%)	NA	NA	6	53
Cd-MOF/S/Ni–NiO	2-Phenoxy-1-phenylethanol (10 mM) in 10 mL solvent; 300 W Xe lamp with cut-off λ > 420 nm	1.058	2-Phenoxy-1-phenylethanone (62%)	NA	6.23	7 h	64
CdS/TiO_2/BC	Aqu. solution of glucose (1 g L^{-1})) and 25 mM NaOH; under 300 W Xe lamp	12.77	Acetic acid (NA)	Acetic acid (63.94)	NA	5 h	48
NaK/C_3N_4-poly(heptazine imide)	80 mg of glucose in KOH; 40 W blue LED (λ = 427 nm)	4.11	Lactic acid (71.2%)	NA	1.66	5	92
0.63%Pt_1/N-CN	50 mg of xylose in aq. KOH (2 mol L^{-1}, 25 mL); 300 W Xe lamp with IR cut off filter	6.8	Lactic acid (89.9%)	Lactic acid (89.8)	21.3	5	104

Table 1 (*continued*)

Photocatalyst	Reaction conditions and light source	H_2 yield (mmol g^{-1} h^{-1})	Value added products (Yield)	Selectivity of major liquid product (%)	AQE (%)	Stability/ cycling stability	Ref.
0.39% Pd_1/g-C_3N_4	2 mg mL^{-1} of fructose in 1.5 mol L^{-1} of NaOH; under 300 W Xe lamp. 1 mg mL^{-1} of xylose in 1.0 mol L^{-1} of NaOH; under 300 W Xe lamp	5.7	Lactic acid (71.8%)	Lactic acid (51)	13.6	5	89
RuP_2/$Ti_4P_6O_{23}$@TiO_2-7	150 mg of arabinose in 5 M KOH; under 10 W visible light	7.0 16.3	Lactic acid (64.1%) Lactic acid (2.41 mmol g^{-1} h^{-1})	Lactic acid (42.5) NA	NA	5	50
TiO_2(Pt)	1 g microcrystalline α-cellulose powder in water; under UV-light irradiation	195.2 mmol	Glucose (0.7 μmol)	NA	NA	7	47
h-ZnSe/Pt@TiO_2	Aqu. solution of α-cellulose; Xe arc lamp (300 W)	1.858	Formic acid (1.1 μmol) Formic acid (372 μmol g^{-1} h^{-1})	NA	2.77	300 h	52
CuS/TiO_2	500 μL H_2O + 400 μL benzylamine in 50 mL DMF; UV-vis light (320–780 nm) by a 300 W Xe lamp	0.7058	*N*-Benzylidenebenzylamine (881.3 μmol h^{-1} g^{-1})	*N*-Benzylidene benzylamine (> 99)	NA	8 h	51

AQE-apparent quantum efficiency.

with a co-catalyst enhances the visible light absorption and charge separation efficiency, and hence, the overall photoredox efficiency; this approach overcomes many of the deficiencies like high charge recombination. Sulphide-based materials show high performance in the co-production of H_2 and VAPs due to its narrow E_g and suitable band edge positions. However, their studies are limited to few biomass components like benzyl alcohol. Dual functional sulphide-based catalysts with high photoredox efficiencies, such as, $ZnIn_2S_4$, are gaining great attention. Nonetheless, under-utilization of holes is likely to photocorrode the sulphides, and hence, care must be exercised. Due to the unique and favorable electrical and optical properties, carbon-based photocatalysts have shown high performance for the parallel production of H_2 and VAPs; however, limited reports are available with sulfide- and carbon-based catalysts.

Overall photoredox reactions involving H_2 production and biomass-component-based oxidation could address the carbon-neutral economy by recycling the biomass, and hence, play a vital role in the future. Although the co-production of H_2 and VAPs by photocatalysis is a promising approach to effectively utilize solar energy and biomass resources, the efficiency of these photoredox reactions should improve further. Fig. 19 shows the main challenges in the photocatalytic H_2 production coupled with biomass oxidation. The following aspects may be considered to improve the widespread applications of this field:

(1) Integration, particularly structural and electronic integration, of constituent components of composite photocatalyst appears to be the key for enhancing photocatalytic activity, as it enhances charge separation and their diffusion to the redox sites. Hence, synthesis strategies need to be customized and evolve for different photocatalyst systems; SILAR appears to be one of the very promising methods. A combination of thin film and SILAR methods is a possibility to scale up the photocatalyst panels to be directly deployed in sunlight.

(2) Unlike a highly alkaline medium employed in biomass component-based electrolysis,[16,34] photocatalysis experiments are carried out around neutral pH = 7, and hence no need of neutralization of bases. However, the efficiency of photocatalysis needs to improve to the acceptable level, which will invite commercial interest to take it ahead to the practical deployment.

(3) Most of the reported photoredox catalysts used for the reactions are in powder form, which limits the light absorption and reusability. By employing a thin-film form of the catalyst, it is possible to improve the photocatalytic efficiency and reusability of the material. Hence, different ways of making desired thin films of photocatalyst materials need to be developed and evaluated.

(4) While anaerobic and aerobic conditions lead to large and small amounts of green H_2, the latter one leads to a larger extent of oxidized products. A combination of N_2 + O_2, either as a mixture or in steps (N_2 followed by O_2 and *vice versa*), could tune the nature of reaction and possibly product selectivity, and increase the scope of the reaction. More efforts are needed in this direction.

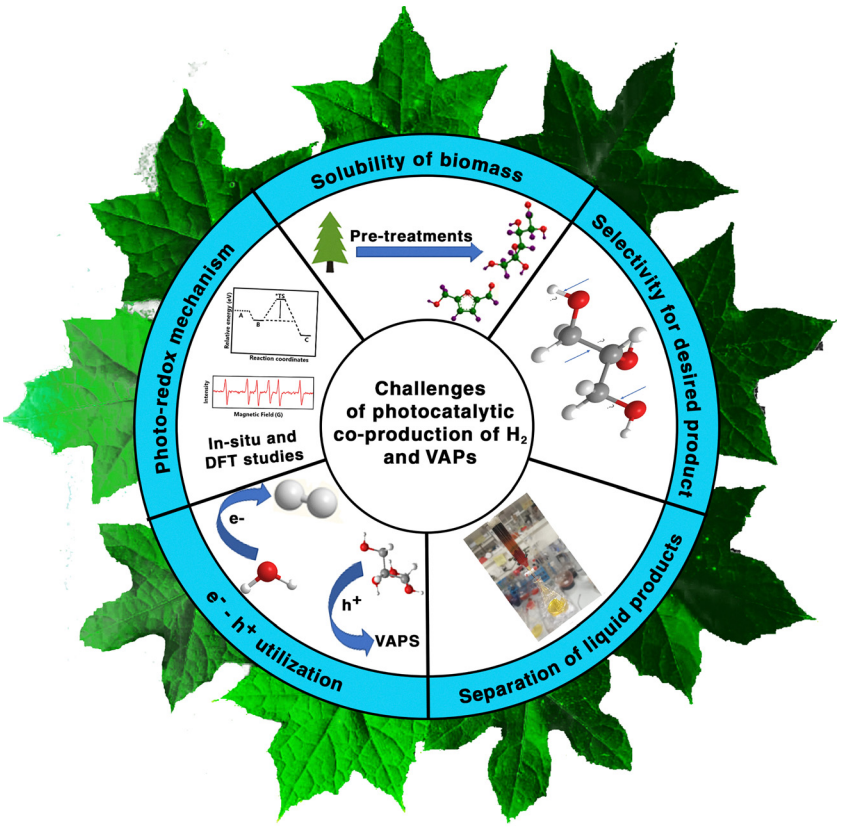

Fig. 19 Major challenges in in the photocatalytic H_2 production coupled with biomass oxidation.

(5) Although the oxidation potential of most of the biomass components is lower than that of water, until now only few biomass component molecules are employed with water for photoredox reactions. In order to expand the versatility of coupled photoredox reactions, more biomass components that are soluble in water have to be explored. Efforts may also be directed to find out the dissolution of high-molecular-weight long-chain components, such as cellulose, in water around neutral pH.

(6) Many photocatalysts produce different sets of products for the same feedstock molecule, like glycerol and glucose. This is mainly due to different extents of C–C cleavage of the input feed molecules. Hence, a significant challenge is present in tuning the selectivity to the desired or relevant product while suppressing the minor ones.

(7) While C–C cleavage is well known in the photocatalysis of biomass-based component molecules, very few reports are present for C–C coupled products to make longer chain molecules in the liquid phase, such as gasoline and diesel; Pd-based co-catalysts may be evaluated. Efforts may be contributed in such areas too.

(8) Biomass components often contain multiple functional groups with a complex structure, and its oxidation generally leads to multiple products. While hydroxyl groups in biomass components are considered as a serious problem in catalytic biomass valorization, photocatalysis exploits the same and oxidizes further to the VAPs. However, fine-tuning the reaction conditions, such as anaerobic/aerobic conditions, temperature and/or pH control, is highly preferred to increase the selectivity of the desired product.

(9) Biomass conversion efficiency in photoredox reactions is low compared to other reactions such as electrocatalysis. The design of the photocatalyst material with photothermal efficiency and high efficiency to absorb near-infrared (NIR) radiations from sunlight is a promising way to enhance the conversion efficiency.

(10) Separation of products, from the reaction mixture, is one of the critical issues, and it is yet to be addressed. While improving the product selectivity efforts by various methods should go on, the development of viable and energy-efficient product separation methods is an urgent requirement.

(11) *In situ* spectral studies of photoredox reactions involving H_2 production and VAPs are very limited; however, they are critical to identify the reaction intermediates and mechanism of photoredox reactions. Exploring more *in situ* spectral studies with relevant spectroscopy to identify the physical and chemical changes of photocatalyst is highly preferred.

(12) A rational thinking on the choice of photocatalysts and co-catalysts, and their integration for the conversion of a given biomass component molecule to the desired product should evolve, based on the redox potential and other experimental factors. DFT calculations could be of immense help.

Author contributions

Sivaraj Rajendran: writing – original draft, writing – review & editing, Simi Saju: writing – review & editing, Thomas Mathew: writing – review & editing, Chinnakonda S. Gopinath: conceived the original idea of review, writing – review & editing.

Conflicts of interest

There are no conflicts to declare.

Data availability

No new primary research data were generated or included as part of this review article.

Acknowledgements

S. R. thanks UGC for the research fellowship. S. R., S. S. and T. M. gratefully acknowledge DST, New Delhi, for the facility support under the DST-FIST program in St. John's College, Anchal, Kerala, India.

References

1 M. Y. Qi, M. Conte, M. Anpo, Z. R. Tang and Y. J. Xu, *Chem. Rev.*, 2021, **121**, 13051–13085.
2 C. S. Gopinath and N. Nalajala, *J. Mater. Chem. A*, 2021, **9**, 1353–1371.
3 (*a*) J. Teng, W. Li, Z. Wei, D. Hao, L. Jing, Y. Liu, H. Dai, Y. Zhu, T. Ma and J. Deng, *Angew. Chem., Int. Ed.*, 2024, **63**, e202416039; (*b*) S. Rajaambal, K. Sivaranjani and C. S. Gopinath, *J. Chem. Sci.*, 2015, **127**, 33–47.
4 (*a*) A. Anantha Krishnan, A. K. Aneesh, R. B. Nair, R. Sivaraj, A. Lamiya, P. K. Jishnu, S. Kurian, T. Mathew, M. Ameen Sha and P. S. Arun, *New J. Chem.*, 2022, **46**, 22256–22267; (*b*) H. Liu, C. Xu, D. Li and H. Jiang, *Angew. Chem., Int. Ed.*, 2018, **57**, 5379–5383; (*c*) K. Sivaranjani, S. Agarkar, S. B. Ogale and C. S. Gopinath, *J. Phys. Chem. C*, 2012, **116**, 2581–2587.
5 T. R. Nivedhitha, H. Bajpai, J. V. Oommen, A. Abraham, I. Chauhan and C. S. Gopinath, *ACS Sustainable Chem. Eng.*, 2024, **12**, 14841–14853.
6 A. Mathew, S. Rajendran, T. Mathew and N. R. Shiju, *Energy Chem.*, 2025, **7**, 100161.
7 (*a*) R. B. Nair, A. A. Krishnan, Aneesh Kumar M. A., S. Rajendran, S. Harikumar, Vidhya C., M. Ameen Sha, T. Mathew, S. Kurian and P. S. Arun, *Energy Adv.*, 2024, **3**, 2790–2800; (*b*) A. A. Krishnan, R. B. Nair, Aneesh Kumar M. A., S. Harikumar, Aleena G., S. Rajendran, S. Kurian, T. Mathew, M. Ameen Sha and P. S. Arun, *J. Mater. Chem. A*, 2025, **13**, 28593–28603.
8 (*a*) M. Kim, A. Razzaq, Y. K. Kim, S. Kim and S. Il In, *RSC Adv.*, 2014, **4**, 51286–51293; (*b*) S. B. Waghmode, R. Vetrivel, S. G. Hegde, C. S. Gopinath and S. Sivasanker, *J. Phys. Chem. B*, 2003, **107**, 8517–8523.
9 International Energy Agency (IEA), *Glob. Hydrog. Rev. 2024*, 2024, pp. 1–293.
10 H. Bajpai, T. R. Nivedhitha, E. Dais, S. S. Kanungo and C. S. Gopinath, *J. Catal.*, 2024, **437**, 115644.
11 S. Sorooshian, *J. Cleaner Prod.*, 2024, **453**, 142272.
12 K. N. Salgaonkar, H. Bajpai, N. B. Mhamane, N. Nalajala, I. Chauhan, K. Thakkar, K. Joshi and C. S. Gopinath, *J. Mater. Chem. A*, 2023, **11**, 15168–15182.
13 Z. Wei, M. Xu, J. Liu, W. Guo, Z. Jiang and W. Shangguan, *Chin. J. Catal.*, 2020, **41**, 103.
14 S. S. Mani, S. Rajendran, T. Mathew and C. S. Gopinath, *Energy Adv.*, 2024, **3**, 1472–1504.
15 M. Wang, H. Zhou and F. Wang, *Joule*, 2024, **8**, 604–621.
16 I. Chauhan, H. Bajpai, B. Ray, S. K. Kolekar, S. Datar, K. K. Patra and C. S. Gopinath, *ACS Appl. Mater. Interfaces*, 2024, **16**, 26130–26141.
17 (*a*) S. Rajaambal, M. Mapa and C. S. Gopinath, *Dalton Trans.*, 2014, **43**, 12546–12554; (*b*) P. A. Bharad, K. Sivaranjani and C. S. Gopinath, *Nanoscale*, 2015, **7**, 11206–11215; (*c*) A. Dubey, A. K. Mishra, S. S. Negi and C. S. Gopinath, *J. Chem. Sci.*, 2022, **134**, 61.
18 L. Luo, W. Chen, S. M. Xu, J. Yang, M. Li, H. Zhou, M. Xu, M. Shao, X. Kong, Z. Li and H. Duan, *J. Am. Chem. Soc.*, 2022, **144**, 7720–7730.
19 I. Chauhan, K. K. Patra, H. Bajpai, N. B. Mhamane, K. N. Salgaonkar and C. S. Gopinath, *Dalton Trans.*, 2023, **52**, 2051–2061.
20 V. Navakoteswara Rao, T. J. Malu, K. K. Cheralathan, M. Sakar, S. Pitchaimuthu, V. Rodríguez-González, M. Mamatha Kumari and M. V. Shankar, *J. Environ. Manage.*, 2021, **284**, 111983.
21 J. Rajagopal, K. P. Gopinath, A. Krishnan, N. Vikas Madhav and J. Arun, *Bioresour. Technol.*, 2021, **321**, 124529.
22 X. Wu, J. Li, S. Xie, P. Duan, H. Zhang, J. Feng, Q. Zhang, J. Cheng and Y. Wang, *Chem*, 2020, **6**, 3038–3053.
23 L. Llatance-Guevara, N. E. Flores, G. O. Barrionuevo and J. L. Mullo Casillas, *Catalysts*, 2022, **12**, 1091.
24 G. Dodekatos and H. Tüysüz, *Catal. Sci. Technol.*, 2016, **6**, 7307–7315.
25 L. Shiamala, K. Vignesh and B. M. Jaffar Ali, *Fuel*, 2023, **333**, 126332.
26 (*a*) M. Muscetta, R. Andreozzi, L. Clarizia, I. Di Somma and R. Marotta, *Int. J. Hydrogen Energy*, 2020, **45**, 28531–28552; (*b*) K. Maeda and K. Domen, *J. Phys. Chem. Lett.*, 2010, **1**, 2655–2661; (*c*) D. Bahnemann, P. Robertson, C. Wang, W. Choi, H. Daly, M. Danish, H. de Lasa, S. Escobedo, C. Hardacre, T. H. Jeon, B. Kim, H. Kisch, W. Li, M. Long, M. Muneer, N. Skillen and J. Zhang, *JPhys Energy*, 2023, **5**, 012004; (*d*) U. Maitra, S. R. Lingampalli and C. N. R. Rao, *Curr. Sci.*, 2014, **106**, 518–527.
27 (*a*) A. Kudo and Y. Miseki, *Chem. Soc. Rev.*, 2009, **38**, 253–278; (*b*) Y. Ma, X. Wang, Y. Jia, X. Chen, H. Han and C. Li, *Chem. Rev.*, 2014, **114**, 9987–10043; (*c*) R. M. Navarro Yerga, M. C. Álvarez Galván, F. del Valle, J. A. Villoria de la Mano and J. L. G. Fierro, *ChemSusChem*, 2009, **2**, 471–485; (*d*) F. E. Osterloh, *Chem. Soc. Rev.*, 2013, **42**, 2294–2320.
28 P. K. Sahu, A. Champati, A. Pradhan and B. Naik, *Sustainable Energy Fuels*, 2024, **8**, 1872–1917.
29 Y. Zhang, H. Yu, R. Zhai, J. Zhang, C. Gao, K. Qi, L. Yang and Q. Ma, *Molecules*, 2023, **28**, 8011.
30 S. Rajendran, S. Saju, S. S. Mani, A. K. Asoka, A. Saha, P. S. Arun, B. Ghosh, T. Mathew and C. S. Gopinath, *J. Mater. Chem. A*, 2025, **13**, 2105–2120.
31 (*a*) Govindjee, D. Shevela and L. O. Björn, *Photosynth. Res.*, 2017, **133**, 5–15; (*b*) K. Qi, C. Imparato, O. Almjasheva, A. Khataee and W. Zheng, *J. Colloid Interface Sci.*, 2024, **675**, 150–191.
32 S. Chu, Y. Pan, Y. Wang, H. Zhang, R. Xiao and Z. Zou, *J. Mater. Chem. A*, 2020, **8**, 14441–14462.
33 (*a*) I. Chauhan, P. M. Vijay, R. Ranjan, K. K. Patra and C. S. Gopinath, *ACS Mater. Au*, 2024, **4**, 500–511; (*b*) A. Saha, V. Murugiah, J. Kollenteakathootu and C. S. Gopinath, *ACS Sustainable Chem. Eng.*, 2025, **13**, 11458–11473.
34 A. Saha, V. Murugiah, R. Ranjan, I. Chauhan, K. K. Patra, H. Bajpai, A. Saha and C. S. Gopinath, *Sustainable Energy Fuels*, 2024, **8**, 2954–2968.
35 S. Kampouri and K. C. Stylianou, *ACS Catal.*, 2019, **9**, 4247–4270.
36 A. Balapure, J. Ray Dutta and R. Ganesan, *RSC Appl. Interfaces*, 2024, **1**, 43–69.
37 A. Fujishima and K. Honda, *Nature*, 1972, **238**, 37–38.
38 S. S. Mani, R. Sivaraj, P. S. Arun, A. Vijayakumar, T. Mathew and C. S. Gopinath, *Energy Adv.*, 2024, **3**, 829–840.
39 X. Du, W. Xie, Y. Wang, H. Li, J. Li, Y. Li, Y. Song, Z. Li, J. Y. Lee and M. Shao, *AIChE J.*, 2024, **70**, e18469.
40 H. Bajpai, I. Chauhan, K. N. Salgaonkar, N. B. Mhamane and C. S. Gopinath, *RSC Sustainability*, 2023, **1**, 481–493.
41 W. Sun, Y. Zheng and J. Zhu, *Mater. Today Sustain.*, 2023, **23**, 100465.

42 S. Rajendran, S. S. Mani, T. R. Nivedhitha, A. K. Asoka, P. S. Arun, T. Mathew and C. S. Gopinath, *ACS Appl. Energy Mater.*, 2024, **7**, 104–116.
43 S. S. Mani, S. Rajendran, S. Saju, B. M. Babu, T. Mathew and C. S. Gopinath, *Chem. – Asian J.*, 2025, **20**, e202401664.
44 S. S. Mani, S. Rajendran, N. Nalajala, T. Mathew and C. S. Gopinath, *Energy Technol.*, 2022, **10**, 2100356.
45 K. K. Patra and C. S. Gopinath, *J. Phys. Chem. C*, 2018, **122**, 1206–1214.
46 A. Akhundi, A. Zaker Moshfegh, A. Habibi-Yangjeh and M. Sillanpää, *ACS ES&T Eng.*, 2022, **2**, 564–585.
47 G. Zhang, C. Ni, X. Huang, A. Welgamage, L. A. Lawton, P. K. J. Robertson and J. T. S. Irvine, *Chem. Commun.*, 2016, **52**, 1673–1676.
48 C. Shi, Y. An, G. Gao, J. Xue, H. Algadi, Z. Huang and Z. Guo, *ACS Sustainable Chem. Eng.*, 2024, **12**, 2538–2549.
49 M. Eisapour, H. Zhao, J. Zhao, T. Roostaei, Z. Li, A. Omidkar, J. Hu and Z. Chen, *J. Colloid Interface Sci.*, 2023, **647**, 255–263.
50 X. Li, Q. Liu, J. Ma, K. Liu, Z. Liu and R. Sun, *J. Mater. Chem. C*, 2023, **11**, 3235–3243.
51 J. Liu, X. Sun, Y. Fan, Y. Yu, Q. Li, J. Zhou, H. Gu, K. Shi and B. Jiang, *Small*, 2024, **20**, 2306344.
52 Y. You, S. Chen, J. Zhao, J. Lin, D. Wen, P. Sha, L. Li, D. Bu and S. Huang, *Adv. Mater.*, 2024, **36**, 2307962.
53 K. N. Salgaonkar, S. R. Kale, N. Nalajala, S. Mansuri and C. S. Gopinath, *Chem. – Asian J.*, 2023, **18**, e202201239.
54 M. Chandra and D. Pradhan, *ChemCatChem*, 2025, **17**, e202500395.
55 (*a*) N. Nalajala, K. N. Salgaonkar, I. Chauhan, S. P. Mekala and C. S. Gopinath, *ACS Appl. Energy Mater.*, 2021, **4**, 13347–13360; (*b*) N. Nalajala, K. K. Patra, P. A. Bharad and C. S. Gopinath, *RSC Adv.*, 2019, **9**, 6094–6100; (*c*) B. Tudu, N. Nalajala, K. Prabhakar Reddy, P. Saikia and C. S. Gopinath, *ACS Sustainable Chem. Eng.*, 2021, **9**, 13915–13925.
56 (*a*) M. Kulkarni-Sambhare, K. N. Salgaonkar, A. Saha and C. S. Gopinath, *ChemCatChem*, 2025, **17**, e00641; (*b*) V. K. Jha, K. N. Salgaonkar, A. Saha, C. S. Gopinath and E. S. S. Iyer, *Nanoscale*, 2025, **17**, 12738–12750.
57 (*a*) G. Z. S. Ling, S. H. W. Kok, P. Zhang, Z.-J. Chiah, L.-L. Tan, B. Chen and W.-J. Ong, *Adv. Funct. Mater.*, 2025, **35**, 2409320; (*b*) M. Mapa, K. Sivaranjani, D. S. Bhange, B. Saha, P. Chakraborty, A. K. Viswanath and C. S. Gopinath, *Chem. Mater.*, 2010, **22**, 565–578.
58 B. Oral, R. Karakoyun, E. Bilgin and R. Yıldırım, *Int. J. Hydrogen Energy*, 2025, **142**, 1014–1025.
59 M. M. Khan and A. Rahman, *Catalysts*, 2022, **12**, 1338.
60 A. Rahman and M. M. Khan, *New J. Chem.*, 2021, **45**, 19622–19635.
61 (*a*) A. Rahman, J. R. Jennings, A. L. Tan and M. M. Khan, *ACS Omega*, 2022, **7**, 22089–22110; (*b*) P. Devaraji, M. Mapa, H. A. Hakkeem, V. Sudhakar, K. Krishnamoorthy and C. S. Gopinath, *ACS Omega*, 2017, **2**, 6768–6781; (*c*) N. Yang, Z. Yin, Z. Chen, C. Gao, Z. Cao, Y. Zheng, Z. Pan, H. Cao, S. Ye and Y. Xiong, *Angew. Chem., Int. Ed.*, 2025, **64**, e202502202; (*d*) W. Liu, Y. Wang, H. Huang, J. Wang, G. He, J. Feng, T. Yu, Z. Li and Z. Zou, *J. Am. Chem. Soc.*, 2023, **145**, 7181–7189.
62 (*a*) C. Long, X. Dong and J. Huang, *Energy Fuels*, 2023, **37**, 136–158; (*b*) K. K. Patra, B. D. Bhuskute and C. S. Gopinath, *Sci. Rep.*, 2017, **7**, 6515; (*c*) Z. Liu, Z. Yu, S. Li, J. Pang, Y. Wang, Z. Wu, S. Liu and R. Tan, *Chem. Commun.*, 2025, **61**, 12179–12182; (*d*) H. Wang, Y. Wan, S. Yin, M. Xu, X. Zhao, X. Liu, X. Song, H. Wang, C. Zhu and P. Huo, *Chem. Commun.*, 2023, **59**, 9356–9359; (*e*) A. Gautam, S. Sk, A. Tiwari, B. M. Abraham, V. Perupogu and U. Pal, *Chem. Commun.*, 2021, **57**, 8660–8663.
63 S. Liu, B. Zhang, Z. Yang, Z. Xue and T. Mu, *Green Chem.*, 2023, **25**, 2620–2628.
64 Y. Zhang, A. Hassan, J. Li and J. Wang, *Catal. Sci. Technol.*, 2025, **15**, 1594–1603.
65 G. Han, Y. H. Jin, R. A. Burgess, N. E. Dickenson, X. M. Cao and Y. Sun, *J. Am. Chem. Soc.*, 2017, **139**, 15584–15587.
66 B. Liu, Y. Li, Y. Guo, Y. Tang, C. Wang, Y. Sun, X. Tan, Z. Hu and T. Yu, *ACS Nano*, 2024, **18**, 17939–17949.
67 Y. Han, Y. Chu, L. Ye, T. Gong, X. Lu and Y. Fu, *Adv. Funct. Mater.*, 2025, **35**, 2411991.
68 Y. Han, Y. Zhang, L. Ye, T. Gong, X. Lu, N. Yan and Y. Fu, *Adv. Funct. Mater.*, 2025, **35**, 2425473.
69 S. Dhingra, T. Chhabra, V. Krishnan and C. M. Nagaraja, *ACS Appl. Energy Mater.*, 2020, **3**, 7138–7148.
70 H. F. Ye, R. Shi, X. Yang, W. F. Fu and Y. Chen, *Appl. Catal., B*, 2018, **233**, 70–79.
71 W. Kang, X. Li, X. Zeng, H. Wu, Y. Ge, L. Yuan, Y. Liu and C. Han, *Chem. Commun.*, 2024, **60**, 10572–10575.
72 R. Du, C. Wang, L. Guo, R. A. Soomro, B. Xu, C. Yang, F. Fu and D. Wang, *Small*, 2023, **19**, 2302330.
73 N. Luo, T. Hou, S. Liu, B. Zeng, J. Lu, J. Zhang, H. Li and F. Wang, *ACS Catal.*, 2020, **10**, 762–769.
74 G. Zhang, S. Huang, X. Li, D. Chen, N. Li, Q. Xu, H. Li and J. Lu, *Appl. Catal., B*, 2023, **331**, 122725.
75 P. Zhang, P. Guo, M. Zhang, X. Qiao, R. Wang, Z. Zhang and S. Qiu, *Chem. Eng. J.*, 2024, **479**, 147265.
76 H. Zhao, C. F. Li, X. Yong, P. Kumar, B. Palma, Z. Y. Hu, G. Van Tendeloo, S. Siahrostami, S. Larter, D. Zheng, S. Wang, Z. Chen, M. G. Kibria and J. Hu, *iScience*, 2021, **24**, 102109.
77 Q. Wan, E. Cui, T. Tong, Z. Cao, F. Wang, S. Yin, K. Song, W. Jiang, G. Liu and J. Ye, *ACS Nano*, 2025, **19**, 7327–7336.
78 Y. S. Cheng, Z. Y. Xing, X. Zheng, X. D. Xu, Y. S. Kang, D. Yu, K. L. Wu, F. H. Wu, G. Yuan and X. W. Wei, *Int. J. Hydrogen Energy*, 2023, **48**, 5107–5115.
79 T. Zhou, Z. Luo, M. Shi, Y. Zhang, Q. Lu, M. Chen, H. Sun, T. He, J. Zhang, Y. Zhang and Q. Liu, *Appl. Catal., B*, 2025, **370**, 125190.
80 K. Sun, Y. Huang, Q. Wang, W. Zhao, X. Zheng, J. Jiang and H.-L. Jiang, *J. Am. Chem. Soc.*, 2024, **146**, 3241–3249.
81 L. Pan, M. Ai, C. Huang, L. Yin, X. Liu, R. Zhang, S. Wang, Z. Jiang, X. Zhang, J.-J. Zou and W. Mi, *Nat. Commun.*, 2020, **11**, 418.
82 S. Meng, X. Ye, J. Zhang, X. Fu and S. Chen, *J. Catal.*, 2018, **367**, 159–170.
83 (*a*) W. Wang, S. Mei, S. Khan, Y. Hu, L. Sun, M. A. Qaiser, C. Zhu, L. Wang and Q. Liu, *ChemSusChem*, 2024, **17**, e202400575; (*b*) S. Gholap, M. Badiger and C. S. Gopinath, *J. Phys. Chem. B*, 2005, **109**, 13941–13947.
84 B. Sun, M. Ye, Y. Xu, Y. Jiang, D. Hou, X. Qing Qiao, M. Wang, Y. Du and D. S. Li, *Adv. Sci.*, 2025, **12**, 2501931.
85 Z. Wang, D. Zhou, K. Tian, G. Chen, Y. Li, S. F. Liu, S.-T. Lee and J. Yan, *ACS Catal.*, 2025, **15**, 3660–3673.
86 X. Wang, B. Liu, S. Ma, Y. Zhang, L. Wang, G. Zhu, W. Huang and S. Wang, *Nat. Commun.*, 2024, **15**, 2600.
87 J. Zhang, J. Ma, R. Cui, W. Ling, M. Hong and R. Sun, *Chem. Eng. J.*, 2025, **503**, 158427.
88 R. Du, X. Huang, J. Ren, H. Guo, R. A. Soomro, L. Guo, C. Yang and D. Wang, *Appl. Catal., B*, 2025, **361**, 124694.
89 (*a*) M. Ren, Y. Pan, G. Yang, Y. Yang, Y. Guo, J. Meng, D. Song, B. Yang and X. Zhao, *J. Colloid Interface Sci.*, 2025, **686**, 1055–1073; (*b*) P. Devaraji and C. S. Gopinath, *Int. J. Hydrogen Energy*, 2018, **43**, 601–613.
90 V. R. Battula, A. Jaryal and K. Kailasam, *J. Mater. Chem. A*, 2019, **7**, 5643–5649.
91 (*a*) Y. Zheng, X. Liang, Z. Hang, J. Ouyang, J. Xing, X. Guo and Z. Chen, *Chem. Commun.*, 2025, **61**, 13157–13160; (*b*) E. Wang, Y.-C. chu, W. Zhang, Y. Wei, C. Si, R. Palkovits, X.-P. Wu and Z. Chen, *Chin. J. Catal.*, 2025, **74**, 308–318; (*c*) A. Verma, D. K. Chauhan and K. Kailasam, *ACS Sustainable Chem. Eng.*, 2025, **13**, 46–55.
92 X. Zhong, Y. Zhu, Y. Wang, Z. Jia, Q. Sun and J. Yao, *J. Alloys Compd.*, 2025, **1020**, 179351.
93 H. T. Liu, T. J. Lin, D. L. Tsai, C. J. Wu and J. J. Wu, *Mater. Today Energy*, 2024, **45**, 101696.
94 L. Tang, Y. Xu, S. Tang, Y. X. Yu, A. Meng, X. Wang and W. De Zhang, *J. Colloid Interface Sci.*, 2025, **688**, 432–442.
95 R. Pan, X. Ge, Q. Liu, H. Yin, Y. Guo, J. Shen, D. Zhang, P. Chen, J. Yuan, H. Xie and C. Liu, *Adv. Funct. Mater.*, 2024, **34**, 2315212.
96 W. Wang, L. Du, R. Xia, R. Liang, T. Zhou, H. K. Lee, Z. Yan, H. Luo, C. Shang, D. L. Phillips and Z. Guo, *Energy Environ. Sci.*, 2022, **16**, 460–472.
97 A. D. Gaonkar, S. Paniya, S. Kancharlapalli and K. Vankayala, *Sustainable Energy Fuels*, 2024, **8**, 4914–4926.
98 Q. Yang, T. Wang, F. Han, Z. Zheng, B. Xing and B. Li, *J. Alloys Compd.*, 2022, **897**, 163177.
99 X. Li, J. Hu, T. Yang, X. Yang, J. Qu and C. M. Li, *Nano Energy*, 2022, **92**, 106714.
100 E. Wang, A. Mahmood, S. G. Chen, W. Sun, T. Muhmood, X. Yang and Z. Chen, *ACS Catal.*, 2022, **12**, 11206–11215.

101 H. Bajpai, K. K. Patra, R. Ranjan, N. Nalajala, K. P. Reddy and C. S. Gopinath, *ACS Appl. Mater. Interfaces*, 2020, **12**, 30420–30430.
102 Z. Fang, M. Zhou, Z. Lin, C. Yang, Y. Hou, J. C. Yu, J. Zhang and X. Wang, *Appl. Catal., B*, 2024, **353**, 124022.
103 S. Lin, H. Meng, Q. Li, X. Xiao, H. Gu, Y. Xie and B. Jiang, *J. Colloid Interface Sci.*, 2025, **685**, 1154–1163.
104 G. Yang, L. Qin, Y. Pan, X. Gao, X. Liu, Y. Guo and J. Meng, *Chem. Eng. J.*, 2025, **509**, 161407.
105 K. Liu, J. Ma, X. Yang, Z. Liu, X. Li, J. Zhang, R. Cui and R. Sun, *Chem. Eng. J.*, 2022, **437**, 135232.
106 J. Ma, J. Zhang, D. Jin, S. Yao and R. Sun, *J. Environ. Chem. Eng.*, 2022, **10**, 108554.
107 V. C. Nguyen, D. B. Nimbalkar, L. D. Nam, Y. L. Lee and H. Teng, *ACS Catal.*, 2021, **11**, 4955–4967.
108 V.-C. Nguyen, M. Sanoe, N. P. Putri, Y.-L. Lee and H. Teng, *Sustainable Energy Fuels*, 2024, **8**, 1412–1423.